GRADUATE AERONAUTICAL LABORATORIES
CALIFORNIA INSTITUTE of TECHNOLOGY
Pasadena, California 91125

Chemical Reactions in Turbulent Mixing Flows

Paul E. Dimotakis* and Anthony Leonard**

Air Force Office of Scientific Research
Grant No. F49620-94-1-0353
15 June 1994 through 28 February 1998

Final Report

Issued: 28 May 1998
Corrected: 15 September 1998

* John K. Northrop Professor of Aeronautics and Professor of Applied Physics

** Professor, Aeronautics

1998

AFRL-SR-BL-TR-98-

0065

REPORT DOCUMENTATION PAGE

1. AGENCY USE ONLY (Leave blank)	2. REPORT DATE	3. REPORT TYPE AND DATES COVERED
	28May98	Final Technical Report 6/15/94-2/28/98

4. TITLE AND SUBTITLE
(U) Chemical Reactions in Turbulent Mixing Flows

5. FUNDING NUMBERS
PE - 61102F
PR - 2308
SA - BS

G - F49620-94-1-0353

6. AUTHOR(S)
Paul E. Dimotakis and Anthony Leonard

7. PERFORMING ORGANIZATION NAME(S) AND ADDRESS(ES)
Graduate Aeronautical Laboratories
California Institute of Technology
Pasadena, CA 91125

8. PERFORMING ORGANIZATION REPORT NUMBER

9. SPONSORING / MONITORING AGENCY NAME(S) AND ADDRESS(ES)
Air Force Office of Scientific Research
110 Duncan Avenue, B115
Bolling AFB DC 20332-8050

10. SPONSORING / MONITORING AGENCY REPORT NUMBER

11. SUPPLEMENTARY NOTES

12a. DISTRIBUTION / AVAILABILITY STATEMENT
Unrestricted

Approved for public release;
distribution unlimited.

12b. DISTRIBUTION CODE

13. ABSTRACT *(Maximum 200 Words)*

This program focused on fundamental investigations of mixing, chemical-reaction, and combustion processes, in turbulent, subsonic, and supersonic free-shear flows. The program was comprised of an experimental effort; an analytical, modeling, and computational effort; and a diagnostics, instrumentation, and data-acquisition-development effort, with significant progress in each. With regard to gas-phase shear-layer mixing and combustion, effects of inflow/initial conditions, compressibility, and Reynolds number were experimentally investigated and, to a large extent, clarified. New measures to characterize level sets in turbulence were developed and successfully employed to characterize experimental data of liquid-phase turbulent-jet flows as well as three-dimensional direct-numerical-simulation data of Rayleigh-Taylor-instability flows. The computational effort has added to our understanding of the (H2+NO)/F2 chemical system employed in the shear-layer-mixing investigations as well as mixing in high-speed flows, along with further developments in Riemann-Invariant-Manifold gasdynamic simulation techniques and their application to unsteady detonation phenomena. On the diagnostic front, developments in digital imaging and Image Correlation Velocimetry have continued, and been used to investigate turbulent-jet mixing, the unsteady flow over an accelerating airfoil, to mitigate aliasing problems in the computer reconstruction of (2+1)-dimensional isosurface data, and in other applications.

14. SUBJECT TERMS
Turbulence, chemical-reacting flows, combustion, supersonic flow, Detonations, hypersonic propulsion, level sets

15. NUMBER OF PAGES
71

16. PRICE CODE

17. SECURITY CLASSIFICATION OF REPORT	18. SECURITY CLASSIFICATION OF THIS PAGE	19. SECURITY CLASSIFICATION OF ABSTRACT	20. LIMITATION OF ABSTRACT
Unclassified	Unclassified	Unclassified	UL

1. Introduction

The documentation below describes work on, "Chemical Reactions in Turbulent Mixing Flows," performed under sponsorship of AFOSR Grant No. F49620–94–1–0353. This work was focused on fundamental investigations of mixing, chemical-reaction, and combustion processes, in turbulent, subsonic, and supersonic free-shear flows. The program was comprised of

- an experimental effort, in
  - chemically-reacting and non-reacting, subsonic and supersonic turbulent free-shear layers;
  - liquid- and gas-phase turbulent jets discharging in an otherwise quiescent reservoir,
  - preliminary work on transverse jets in a cross-flow, and
  - a study of the flow field over accelerating airfoils;
- an analytical, modeling, and computational effort, focusing on the behavior of hyperbolic systems with strong fronts (shocks/detonations);

and

- a diagnostics, instrumentation, and data-acquisition-development effort.

Parts of this effort were cosponsored by AFOSR URI Grant No. F49620–93–1–0338, on "Interaction of Chemistry, Turbulence, and Shock Waves in Hypervelocity Flow," with some instrumentation support derived from the imaging efforts supported under AFOSR/DURIP Grant No. F49620–95–1–0199. Some experiments were also undertaken as part of work on, "Whole-field measurements of turbulent flow for the study of aero-optical effects," under AFOSR Grant No. F49620–94–1–0283.

The work outlined above is documented in the report that follows, with additional detailed documentation in the publications, theses, and reports that were written in the course of this research program. These are listed in Sec. 10, below.

2. Shear-layer mixing and combustion

The experimental data discussed in this section were investigated in the GALCIT Supersonic Shear-Layer Facility. This unique facility allows the study of high-Reynolds-number, chemically-reacting, turbulent shear-layer flows, by employing the $(H_2 + NO)/F_2$ chemical system for "flip experiments" (Koochesfahani & Dimotakis 1986), in addition to color-schlieren and Rayleigh-laser imaging, for flow visualization. This effort has focused on several aspects of turbulent shear-layer behavior, spanning incompressible- to compressible-flow regimes. In particular, the results of studies on effects of inflow/initial conditions, compressibility, and Reynolds number, will be described in what follows.

As discussed by various authors, *e.g.*, Dimotakis (1986), high-Reynolds-number mixing processes can be conceptually broken into three separate stages: large-scale entrainment, intermediate-scale stirring, and small-scale diffusion/mixing, with each stage important to the overall molecular mixing, and subsequent combustion, of two, initially-separated, freestream fluids.

This sequence can be expressed in terms of the quantities accessible to current measurement techniques, *i.e.*,

$$\frac{\delta_{\rm m}}{x} = \left(\frac{\delta}{x}\right) \times \left(\frac{\delta_{\rm m}}{\delta}\right) , \qquad (1)$$

where $\delta_{\rm m}$ is the equivalent mixed-fluid thickness, and δ the outer-scale thickness. In these experiments, δ_T is employed as a shear-layer thickness measure, defined as the 1% temperature-rise thickness, *i.e.*, the transverse extent of the shear layer which lies within 1% of the maximum temperature rise (Dimotakis 1991a). As such, $\delta_{\rm m}/\delta_T$ represents the fraction of molecularly-mixed fluid in the layer, or equivalently, the molecular-mixing efficiency. The first term represents the first stage of mixing, while the second represents the process at all of the remaining spatial scales, down to the diffusion, or Batchelor, scale. Because of the large dynamic range of spatial scales present in a high-Reynolds-number flow, $\delta_{\rm m}/\delta$ is inaccessible to direct-measurement techniques, *e.g.*, laser-induced fluorescence, and consequently, reliable estimates of molecular mixing must rely on techniques such as the chemically-reacting flip experiments employed here.

2.1 Inflow/initial conditions

A set of experiments was performed to explore effects of inflow conditions, at incompressible-flow conditions. At a (local) Reynolds number of,

$$Re_\delta \equiv \frac{\rho \Delta U \delta(x)}{\mu} \sim 2 \times 10^5 ,$$

and freestream-velocity and -density ratios of,

$$r \equiv U_2/U_1 \simeq 0.4 \qquad \text{and} \qquad s \equiv \rho_2/\rho_1 \simeq 1 ,$$

respectively, the data show a dramatic influence of perturbed inflow conditions on scalar mixing.

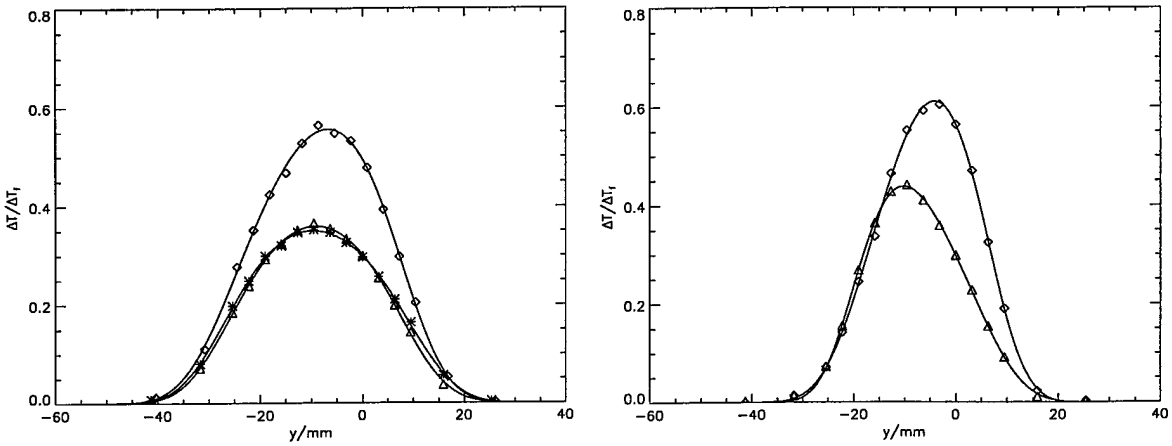

FIG. 1 Normalized temperature-rise data. Left: untripped boundary layers. Right: tripped high-speed boundary layer. Reactant compositions - diamonds: $\phi = 8$; triangles: $\phi = 1/8$; asterisks: $\phi = 1/8$, reduced chemical-kinetic rate.

Two sets of temperature-rise data from such experiments are presented, in Fig. 1, with corresponding color-schlieren flow-visualization data in Fig. 2. The temperature-rise data, in the form of the "flip experiment", provide a resolution-free probe of the molecular-scale mixing, in the fast-kinetic regime.

The only difference between these is the addition of a 0.8 mm-diameter trip wire on the splitter plate (high-speed side), 50 mm upstream of separation. The data are measured far downstream of separation (Bradshaw 1966), $x/\theta_1 \simeq 3300$, where x is the streamwise coordinate and θ_1 is the high-speed boundary-layer momentum thickness, and at a large value of the pairing parameter (Ho & Huang 1982 and Karasso & Mungal 1996), $P \simeq 47$. These measures indicate that the turbulence can be regarded as fully-developed.

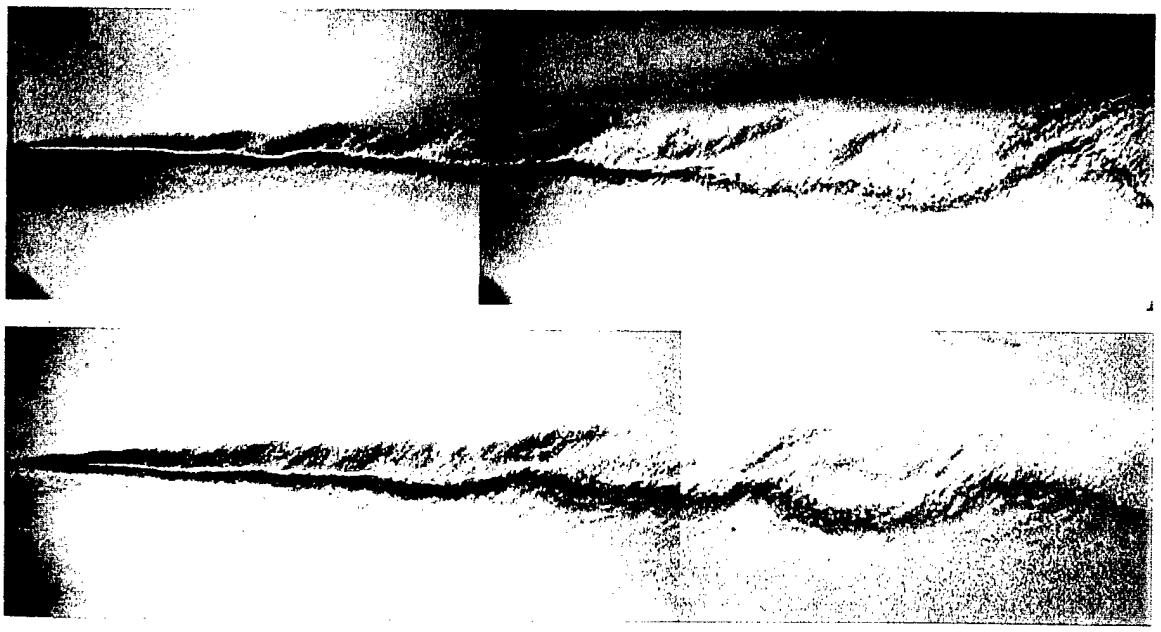

FIG. 2 Color schlieren visualizations of untripped (top) and tripped (bottom) flows. A qualitative difference in visualized-flow structure is evident.

This change in inflow conditions has a significant effect on all scales of the flow: the shear-layer growth rate, δ_T/x, has decreased by 21%; the mixed-fluid fraction δ_m/δ_T, has increased by 11%; and the mixed-fluid composition ratio has decreased by 9%. Additionally, the data indicate a change from a non-marching scalar probability-density function (pdf), to a marching pdf, when the boundary layer was tripped. These observations suggest a shear-layer behavior that depends on not only local-flow properties, but also on upstream conditions, reminiscent of results from low-dimensionality, non-linear (chaotic) systems.

A more complete description of this work can be found in Slessor *et al.* (1998a).

2.2 Compressibility

Compressibility effects on turbulent shear layers are often presented in terms of the total convective Mach number (Papamoschou 1989),

$$M_c \equiv \frac{U_1 - U_2}{a_1 + a_2}, \tag{2}$$

where U_i and a_i are the freestream velocities (speeds) and speeds of sound, respectively. In the following, we evaluate the utility of this parameter, as well as investigate the effect of compressibility on both molecular mixing and flow structure.

2.2.1 Compressibility and growth

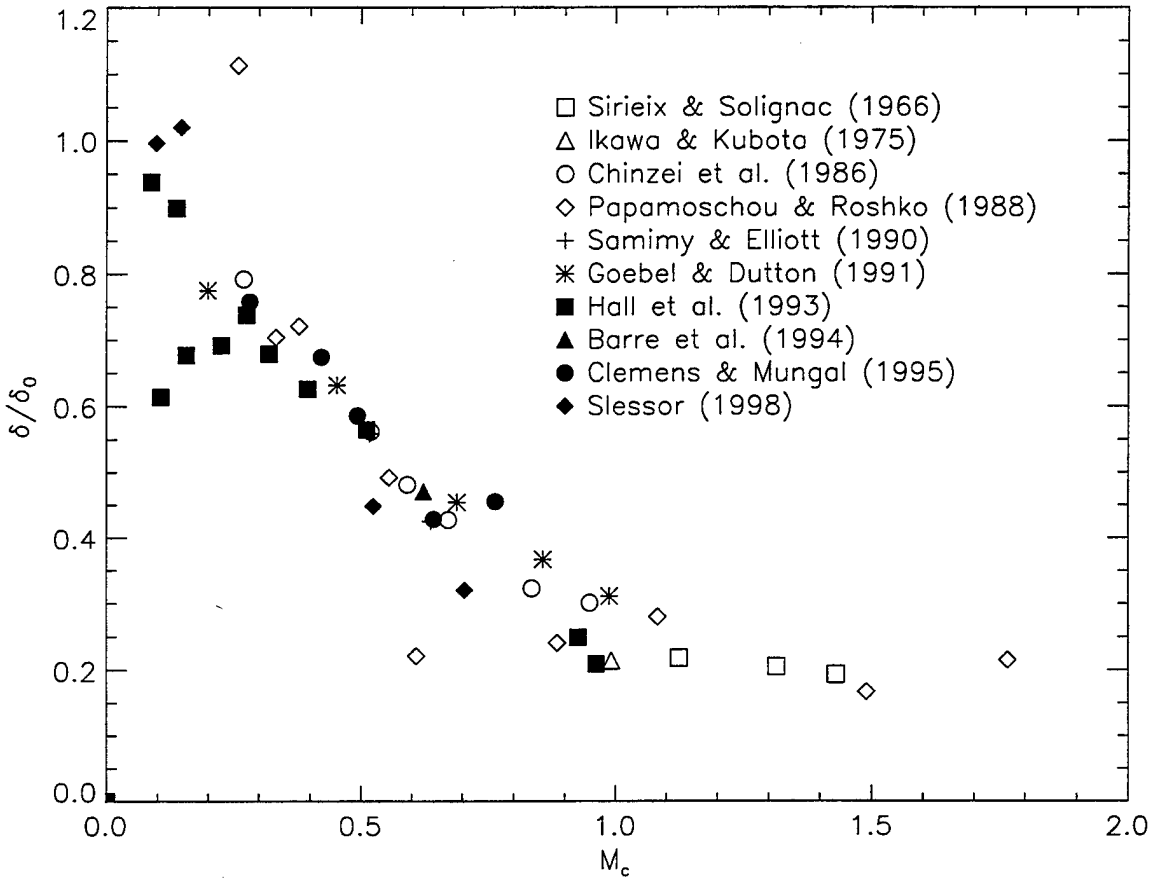

FIG. 3 Normalized compressible shear-layer growth rates as parameterized by the total convective Mach number, M_c (Eq. 2).

It is a well-known experimental fact that compressibility acts to reduce to outer-scale growth rate, $\delta(x)/x$. In particular, compressibility is usually assumed to act independently of freestream-velocity and -density ratios, in the form,

$$\frac{\delta/x}{\delta_0/x} \simeq \frac{\delta}{\delta_0}(M_c) \neq \text{fn}\left(r \equiv \frac{U_2}{U_1}, s \equiv \frac{\rho_2}{\rho_1}\right) , \qquad (3)$$

with estimates for the incompressible-flow growth rate, δ_0/x, used to normalize the (measured) compressible-flow growth rate, δ/x, provided by the spatial-growth model of Dimotakis (1986). Existing compressible-flow data are plotted in this fashion in Fig. 3.

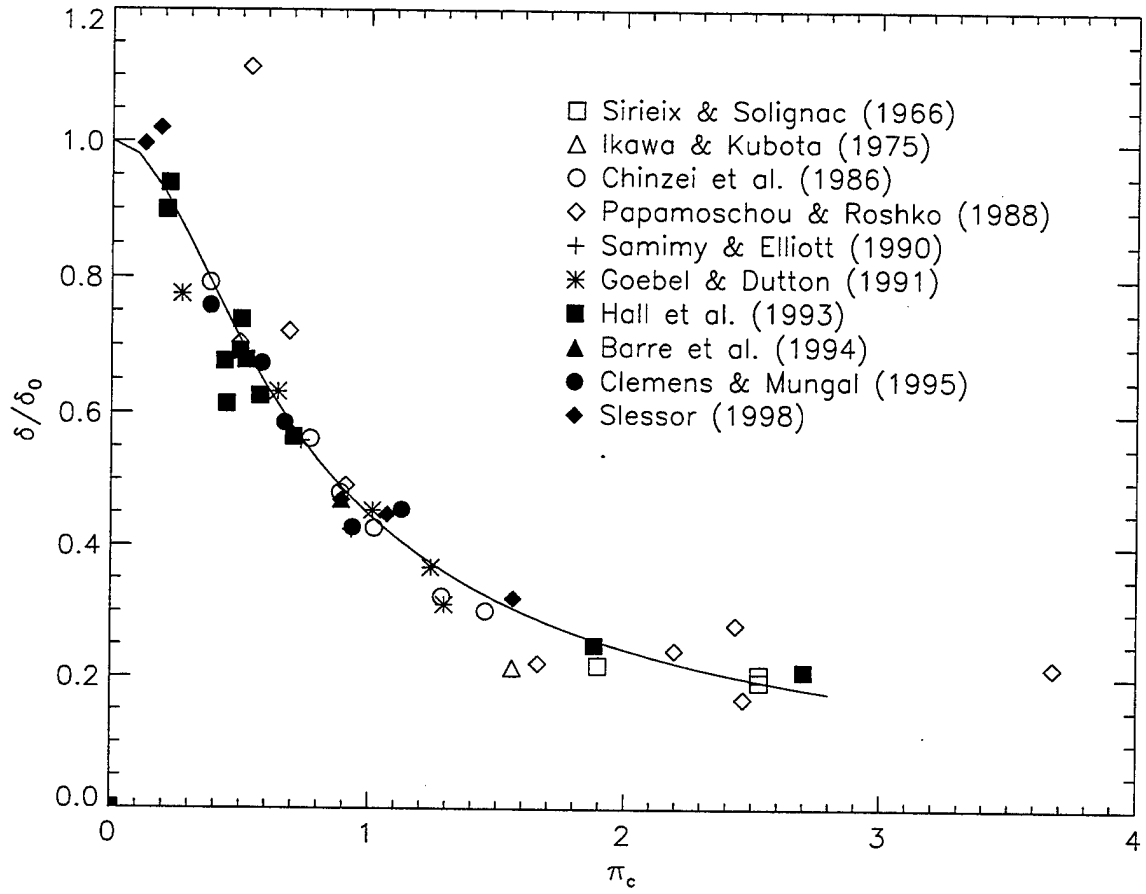

FIG. 4 Normalized (as in Fig. 3) compressible shear-layer growth rates parameterized by the proposed compressibility parameter Π_c (Eq. 4). Solid curve is Eq. 5.

Abnormally-low growth rates are evident in Fig. 3, and suggest either an inaccurate representation of either the incompressible shear-layer growth rate or the flow compressibility. Interestingly, as observed by several authors, *e.g.*, Hall *et al.* (1993) and Lu & Lele (1994), these scaling violations are observed in flows with extreme values of the freestream density ratio, $s \equiv \rho_2/\rho_1$. Existing incompressible growth-rate data (Brown & Roshko 1974) are well-represented by the Dimotakis (1986) model, indicating that M_c provides an inadequate measure of compressibility.

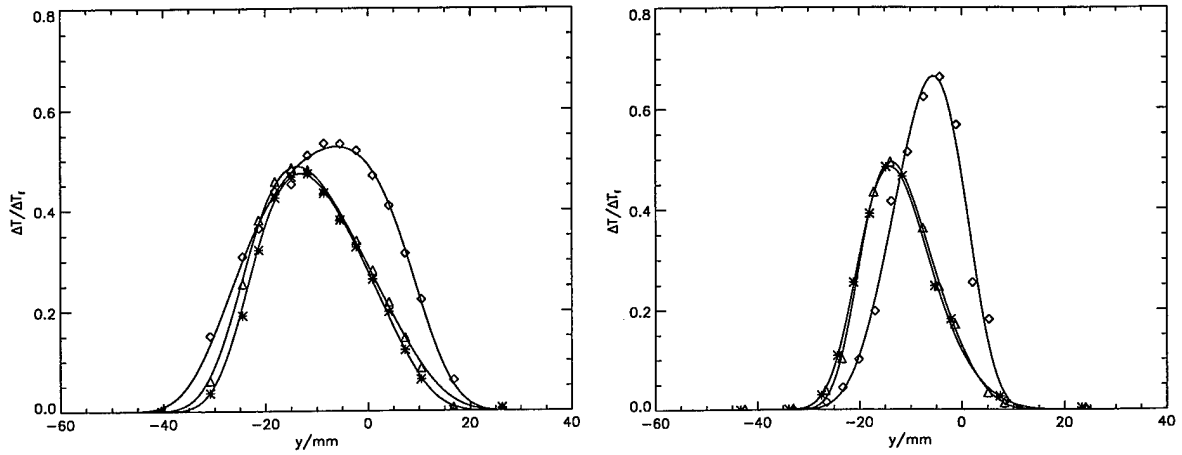

FIG. 5 Normalized temperature-rise data. Left: $M_c \simeq 0.25$, Right: $M_c \simeq 0.47$. Reactant compositions - diamonds: $\phi = 8$; triangles: $\phi = 1/8$; asterisks: $\phi = 1/8$, reduced chemical-kinetic rate.

A new (maximum) compressibility scale has been proposed,

$$\Pi_c = \max_i \left[\frac{\sqrt{\gamma_i - 1}}{a_i} \right] \times \Delta U \,, \tag{4}$$

derived from considerations of compressibility as a kinetic-to-thermal-energy conversion. The experimentally-measured growth rates, normalized as in Fig. 3, are plotted against Π_c in Fig. 4. These data observe a near-functional dependence on this parameter, to a better extent than on M_c, with a solid curve through the data,

$$\frac{\delta}{\delta_0} \simeq \left(1 + \alpha \Pi_c^2\right)^{-\beta} \,, \quad \alpha \simeq 4, \; \beta \simeq 0.5 \,. \tag{5}$$

The systematic deviations observed in flows with extreme density/speed-of-sound ratios are absent when scaled in this fashion.

A more complete discussion of these results is available in Slessor *et al.* (1998b).

2.2.2 Compressibility and mixing

A set of experiments was performed to explore effects of compressibility on molecular mixing. The partition in Eq. 1 indicates that compressibility should result in a *net decrease* in the amount of molecularly-mixed fluid, at least at moderate-to-high compressibility conditions. This expectation stems from two experimental facts (Dimotakis 1991a): the large-scale growth rate is approximately 1/2 of its incompressible value by $M_c \simeq 0.5$, and the mixed-fluid fraction is approximately 1/2 at incompressible-flow conditions.

At nominally-constant values of the (local) Reynolds number,

$$Re_\delta \equiv \frac{\rho \Delta U \delta(x)}{\mu} \sim 9 \times 10^5 ,$$

and freestream-velocity and -density ratios,

$$r \equiv U_2/U_1 \simeq 0.4 \qquad \text{and} \qquad s \equiv \rho_2/\rho_1 \simeq 1 ,$$

respectively, flip experiments were performed at two compressibility levels,

$$M_c \simeq 0.25 \qquad \text{and} \qquad M_c \simeq 0.47 .$$

Temperature-rise data from these two chemically-reacting flip experiments are presented in Fig. 5.

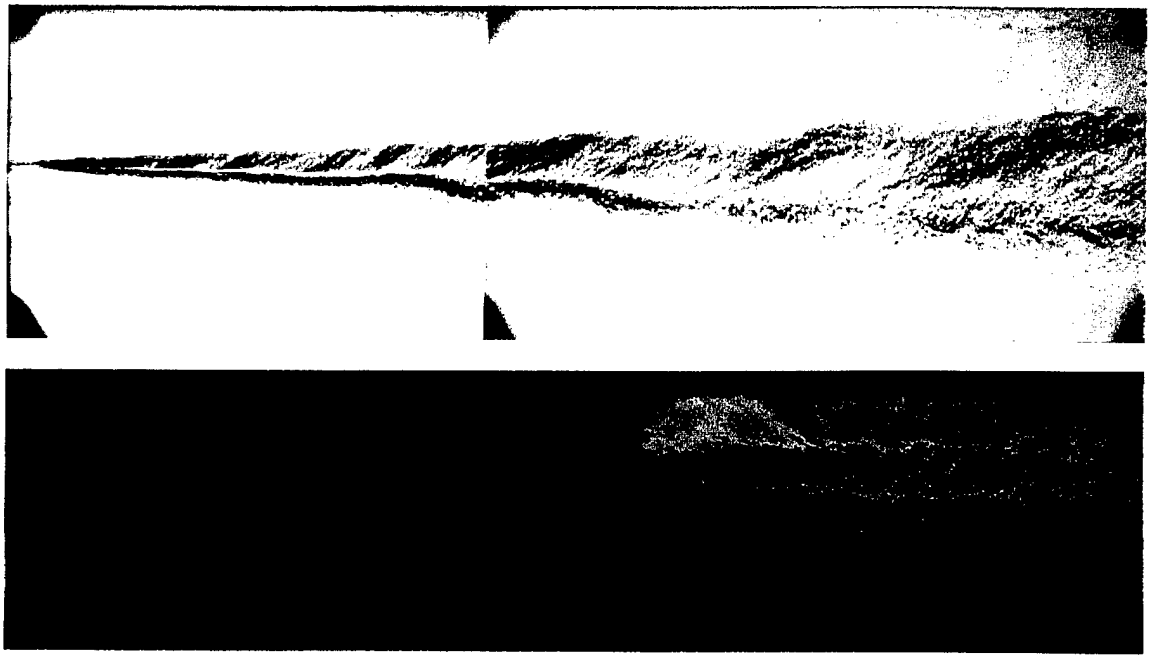

FIG. 6 Color-schlieren visualizations of low-compressibility ($M_c \simeq 0.25$, top) and high-compressibility ($M_c \simeq 0.47$, bottom) flows.

Several differences, attributable solely to the increase in flow compressibility, are noted. In particular, the shear-layer is seen to be thinner, *i.e.*, δ/x has been reduced, at the higher compressibility, in quantitative agreement with previous investigations (Fig. 3). For the H_2-rich ($\phi = 1/8$) parts of the flip experiment, the maximum normalized temperature rises are comparable in both low- and moderate-compressibility flows. However, the maximum attained in the F_2-rich ($\phi = 8$) part is significantly (25%) higher than in low-compressibility flow, reaching nearly 70% of the adiabatic flame temperature for this mixture.

These data, despite the significant increase in normalized temperature-rise at $\phi = 8$, show only a modest increase in mixed-fluid fraction, δ_m/δ_T, associated with the increase in M_c. This reflects a change in the shape of the temperature-rise profile, and consequently, the mixed-fluid structure. Changes are also observed in the instantaneous spanwise-averaged flow visualizations in Fig. 6, where qualitative differences in visualized structure are evident. A modified flow structure is also indicated by the change in the mixed-fluid composition ratio, which is seen to increase for moderate-compressibility flow, favoring the high-speed fluid to a greater extent than in the corresponding low-compressibility flow.

A more complete description of these experiments is available in Slessor (1998).

2.2.3 Compressiblity and flow structure

In order to visualize the instantaneous, spanwise-resolved evolution of the flow structure with increasing compressibility, laser-Rayleigh scattering images were recorded in the midspan plane of three different shear-layer flows. These data complement both the spanwise-integrated color-schlieren data and flip-experiment temperature-rise data described above. The images were recorded with a pulsed (20 ns FWHM duration) Nd:YAG laser-illumination source formed into a light sheet, and a cryogenically-cooled CCD camera. The imaging contrast is provided by the larger index of refraction (scattering cross-section) of C_2H_4, which is used as the low-speed-freestream fluid, in conjunction with the small index of refraction of either N_2, or He, used as the high-speed freestream fluid.

Three sample images, Figs. 7–9, recorded for flows at compressibility levels of $M_c \simeq 0.15$, $M_c \simeq 0.54$, and $M_c \simeq 0.96$, respectively, exhibit a qualitative change with increasing compressibility. In particular, the low-compressibility flow is characterized by typical large-scale, organized "coherent structure", which is less evident at moderate-compressibility conditions, and even less so at high-compressibility conditions. These findings are in qualitative accord with previous investigations, *e.g.*, Clemens & Mungal (1995). In the highest-compressibility flow, a traveling shock-wave system has been captured in the lower, low-speed freestream, and is similar to those observed in spanwise-integrated (schlieren) images, at similar flow conditions (Hall *et al.* 1993). This system is indicative of a well-defined flow structure convecting downstream supersonically with respect to the low-speed freestream.

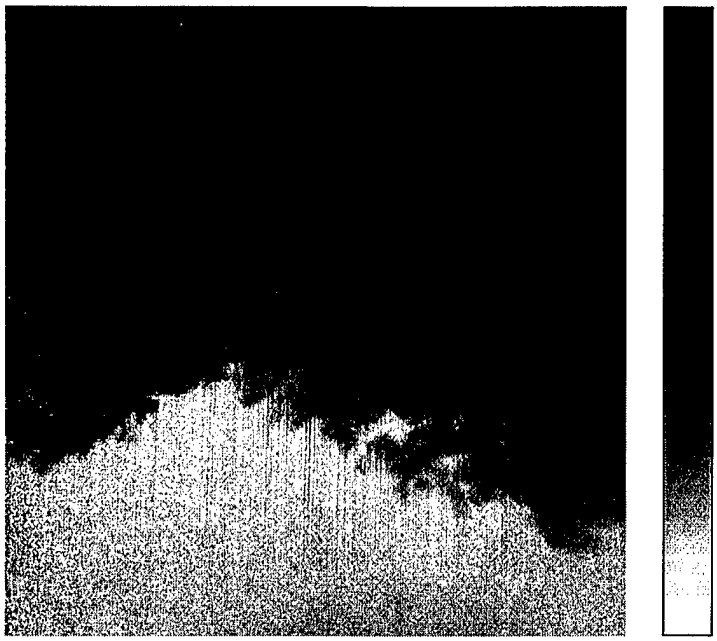

FIG. 7 Rayleigh-scattering visualization of a subsonic shear-layer flow at $M_c \simeq 0.15$. Flow is left-to-right, with the high-speed stream on the top.

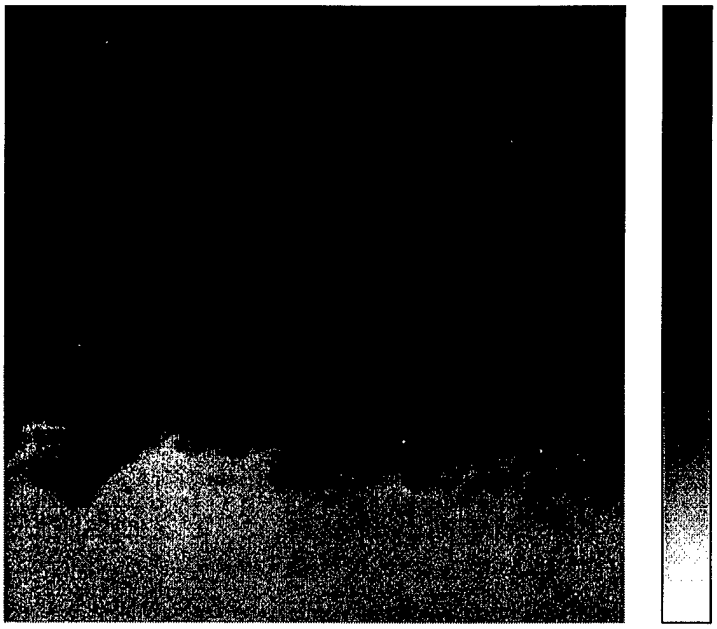

FIG. 8 Rayleigh-scattering visualization of a moderate-compressibility shear-layer flow ($M_1 \simeq 1.5\,\mathrm{N}_2$, $M_c \simeq 0.54$).

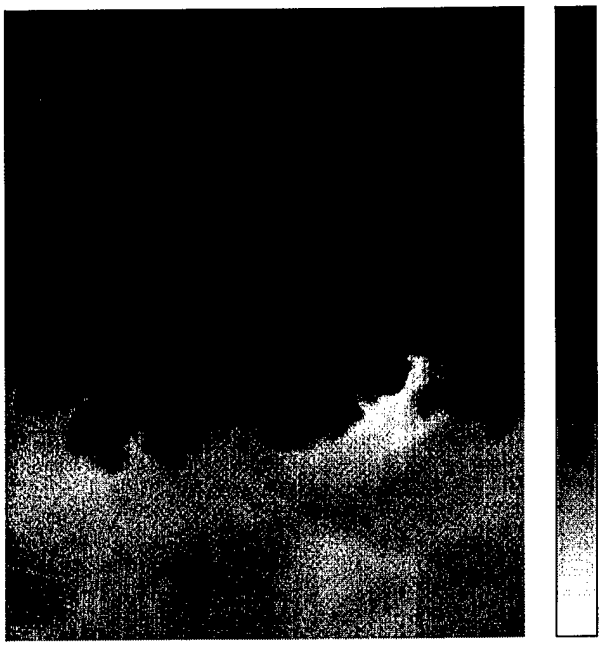

FIG. 9 Rayleigh-scattering visualization of a high-compressibility shear-layer flow ($M_1 \simeq 1.5$ He, $M_c \simeq 0.96$).

Even though a reduction in organization of the scalar field is observed with increasing compressibility, we note the presence of distinct scalar-field interfaces in all images. The presence of such interfacial features is the signature of large-scale entrainment and mixing, in which inducted fluid is nearly homogenized by the turbulent stirring and diffusion processes (Dimotakis 1991a), within boundaries (separatrices) across which transport is impeded. As evident from the image data presented above, these interfaces can be clearly seen in all three compressibility cases investigated.

Further experimental details and a discussion of these investigations in the context of optical-beam propagation and aero-optical phenomena can be found in Dimotakis *et al.* (1998b), which documents parts of our work in aero-optics, "Whole-field measurements of turbulent flow for the study of aero-optical effects".†

† Cofunded by AFOSR Grant No. F49620-94-1-0283.

2.3 Reynolds-number effects

A part of this effort has been to document the effects of viscous diffusion on molecular mixing, at high Reynolds numbers, *i.e.*, $Re_\delta \gg 10^4$ (Dimotakis 1993). Although these effects are expected to be small over the range of Reynolds numbers attainable in the laboratory, the operating range of practical engineering devices spans many orders of magnitude (Dimotakis 1991a) and even a slow, *e.g.*, logarithmic, dependence on Reynolds number can amount to large differences between laboratory-scale and engineering-scale devices.

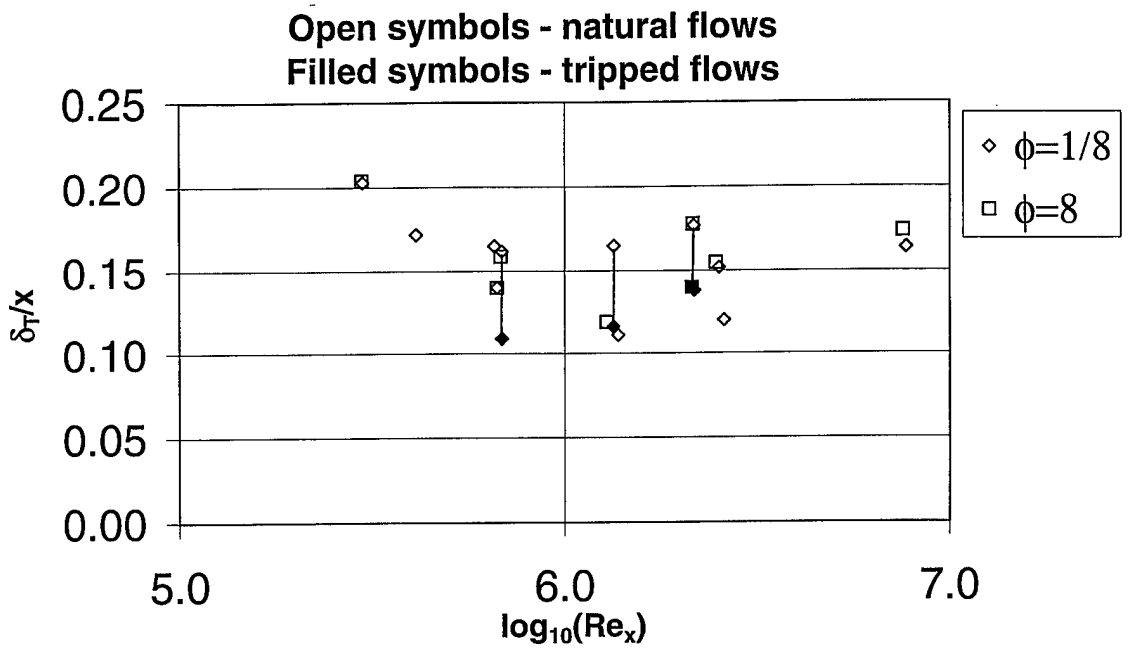

FIG. 10 Shear-layer δ_T thickness (*cf.* Sec. 2) data, for $r \equiv U_2/U_1 \simeq 0.4$ and $s \equiv \rho_2/\rho_1 \simeq 1$, plotted as a function of (the decimal logarithm of) Reynolds number.

Shear-layer growth-rate data, recorded for several different chemically-reacting flows, are shown in Fig. 10, plotted *vs.*

$$Re_x \equiv \frac{\rho U_1 x}{\mu} , \tag{6}$$

where x is the local measuring station, to uncouple changes in the local shear-layer thickness, $\delta(x)$, from other changes in the flow. The difficulty of ascertaining isolated Reynolds numbers effects is evident in this plot. For example, the effect of tripping the high-speed boundary layer (open/filled symbols joined by vertical

lines), is seen to have a more significant effect on the flow than a change of nearly two orders of magnitude in Re_x.

With this caveat, the shear-layer mixed-fluid fraction data are presented in Fig. 11, along with predictions by models of Broadwell, Breidenthal, and Mungal (BBM: Broadwell & Mungal 1991); and of Dimotakis (1987). The inflow-condition experiments described above are joined by a line (tripped flow: filled symbol) to indicate the magnitude of these effects. Results from Island (1997) are also included, along with an estimate for the renormalization required to reconcile their choice of a 5%-scalar-threshold thickness employed in normalizing cold-chemistry data, with the 1%-temperature-rise thickness, δ_T, employed in normalizing chemically-reacting data in the work undertaken as part of this Grant.

It is perhaps difficult to compare the validity of the two models, on the basis of these data alone. However, both models, as well as the data, agree with an overall downward trend of the mixed-fluid fraction, δ_m/δ_T, with increasing Reynolds number.

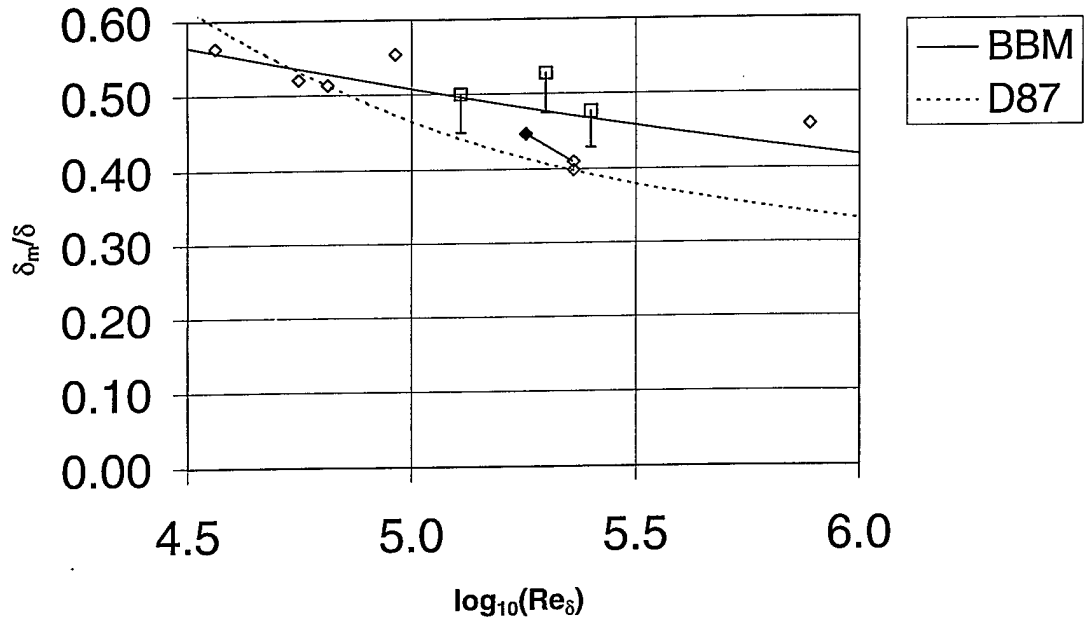

FIG. 11 Shear-layer mixed-fluid fraction, δ_m/δ_T, *vs.* (local) Reynolds numbers, Re_δ, for incompressible flows ($M_c \leq 0.25$). Diamonds: chemically-reacting flows, squares: cold-chemistry flows. Model predictions: solid curve - BBM, dashed curve - D87.

3. Mixing and the geometry of isoscalars in turbulent flows

During this reporting period, an analysis was undertaken to quantify the geometry of isoscalar surfaces derived from scalar-field data in turbulent flows. In particular, the data used were the measurements by Catrakis & Dimotakis (1996a) of mixing in liquid-phase (high-Schmidt-number) turbulent jets and, more recently, three-dimensional DNS data of mixing in Rayleigh-Taylor-instability-driven flows (Cook 1998).

For the jet data, the fluid Schmidt number was $Sc \simeq 2.0 \times 10^3$, with flow Reynolds numbers of $Re \simeq 4.5 \times 10^3$, 9.0×10^3, and 18×10^3. These fluid/flow parameters resulted in a jet-fluid concentration field with a complex, multiscale geometry. Two-dimensional, high-resolution and high-signal-to-noise-ratio images of the scalar far field in this flow were recorded using the laser-induced-fluorescence technique, in a plane normal to the jet axis, and are shown in Fig. 12. They span the whole jet-fluid-concentration field, at the $z/d_j = 275$ downstream measurement location.

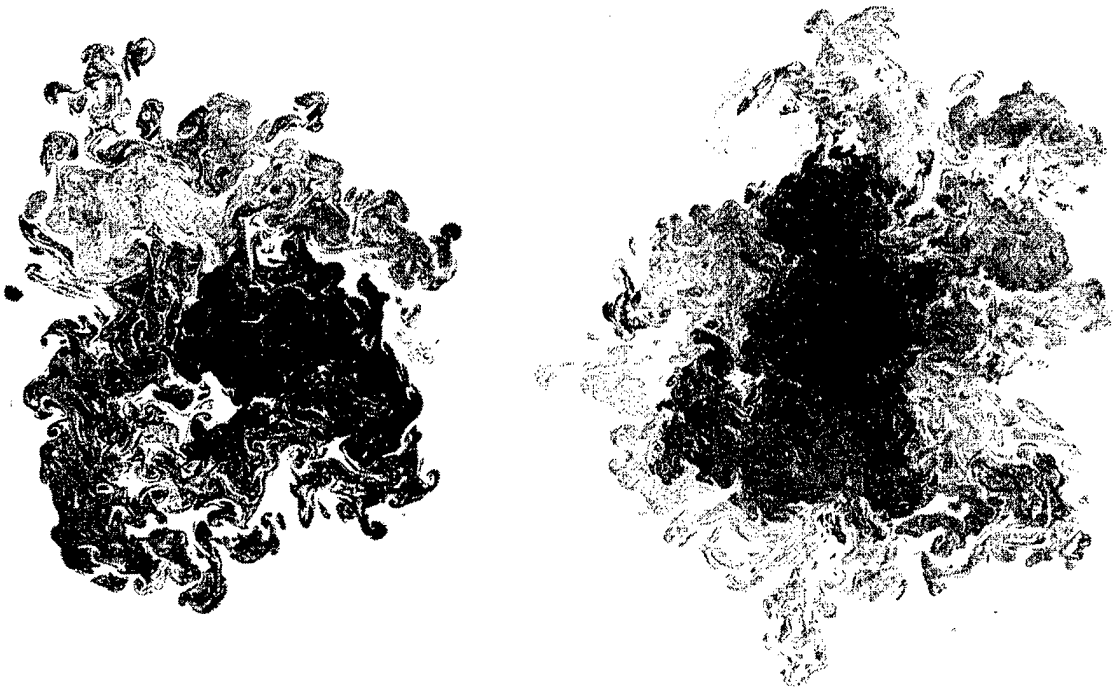

FIG. 12 Laser-induced fluorescence scalar-field data in a liquid-phase turbulent jet at $Re \simeq 4.5 \times 10^3$ (left) and 18×10^3 (right) in a plane normal to the jet axis in the far field ($z/d_j = 275$).

It is interesting to note that classical scalar spectra convey little information regarding geometry of isoscalar surfaces. Spatial spectra computed for the jet scalar-field data are shown in Fig. 13. The 2-D spectrum (left) is for a single-image realization ($Re = 9 \times 10^3$) and can be seen to be very-nearly axisymmetric. Radial spectra, obtained by azimuthal integration, are also shown (right) for the three Reynolds numbers investigated. As can be seen, other than axisymmetry, very little information is conveyed by the 2-D spectrum. A similar lack of information can be noted for the radially-averaged spectra, other than a decreasing wavenumber content with increasing Re, in contrast to classically-expected behavior. The departures in behavior occurs at wavenumbers corresponding to scales roughly 1/3 the image extent and are not the consequence of measurement resolution, which is adequate.

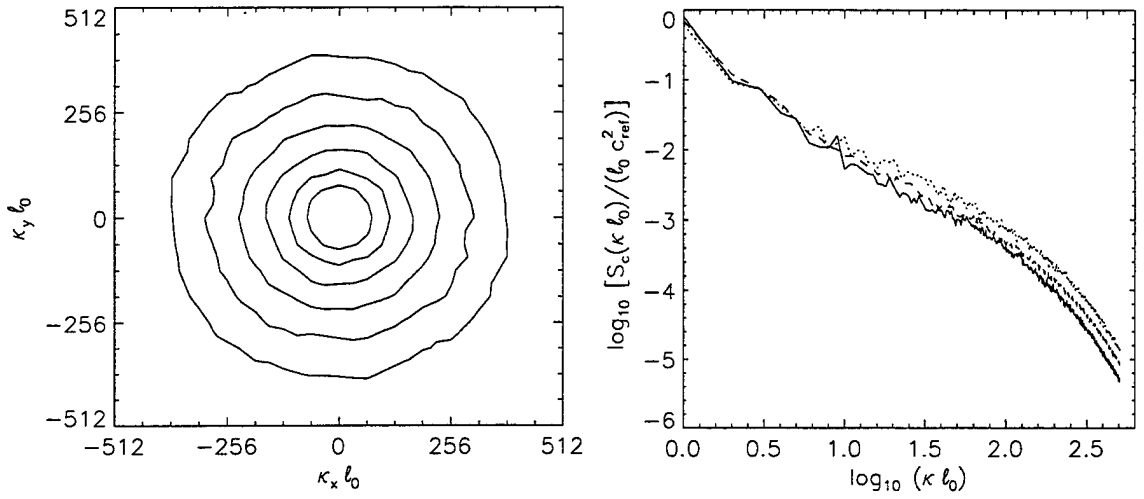

FIG. 13 Scalar spectrum for single realization in a turbulent jet, at $Re = 9 \times 10^3$ (left) and ensemble-averaged radial scalar spectra (right), for $Re = 4.5 \times 10^3$, 9×10^3, and 18×10^3; lines of increasing solidity denote increasing Re.

For the jet isoscalar-surface analysis, the concentration data were thresholded at three scalar levels, $c(x, y) = c_1$, c_2, and c_3, where the c_2 level was chosen to correspond to the peak in the scalar pdf at the two lower Reynolds numbers and the c_1 and c_3 levels span the c_2 level and represent outer and inner contours, respectively (*cf.* Catrakis & Dimotakis 1996a, Fig. 8) The majority of the level-set analysis was performed at the c_2 threshold. One of the most interesting findings is that the coverage length of the isoscalar contours, defined as, $L(\lambda)/\delta_b = \lambda N_2(\lambda)/\delta_b$, *decreases* with increasing Re. This is plotted in Fig. 14 (left). The size, δ_b, of the bounding box partitioned to obtain the coverage counts was independent of Re, within measurement statistics, at the c_2 scalar threshold.

Another finding is that the coverage dimension, $D_2(\lambda)$, is a smoothly-increasing function of scale, bounded by its limiting value of unity (topological dimension), at the smallest scales, and 2 (embedding dimension), at the largest scales, for these data. This behavior persists for all Reynolds numbers investigated and is important implying that previously-reported power-law coverage proposals seriously misrepresent the total length of such contours. Accurate knowledge of such quantities is crucial for the prediction and modeling of mixing, chemical reactions, and combustion in turbulent flows.

Both the coverage length and dimension indicate less-convoluted level sets with increasing Re, in accord with the radially-averaged spatial-spectrum sequence (Fig. 13, right). The limiting value of $L(\lambda)$, as $\lambda \rightarrow 0$, and the coverage dimension, $D_2(\lambda)$, at medium-to-large scales, both decrease with increasing Re. These findings are consistent with *enhanced mixing*, relative to stirring, as Re increases, leading to improved local homogenization of the scalar field and geometrically-simpler scalar level sets. These, in turn, result in lower surface-to-volume ratios, with increasing Re. This is manifest in the comparison plot of sample c_2-level sets computed from $Re = 4.5 \times 10^3$ (left) and $Re = 18 \times 10^3$ (right) realizations (Fig. 15).

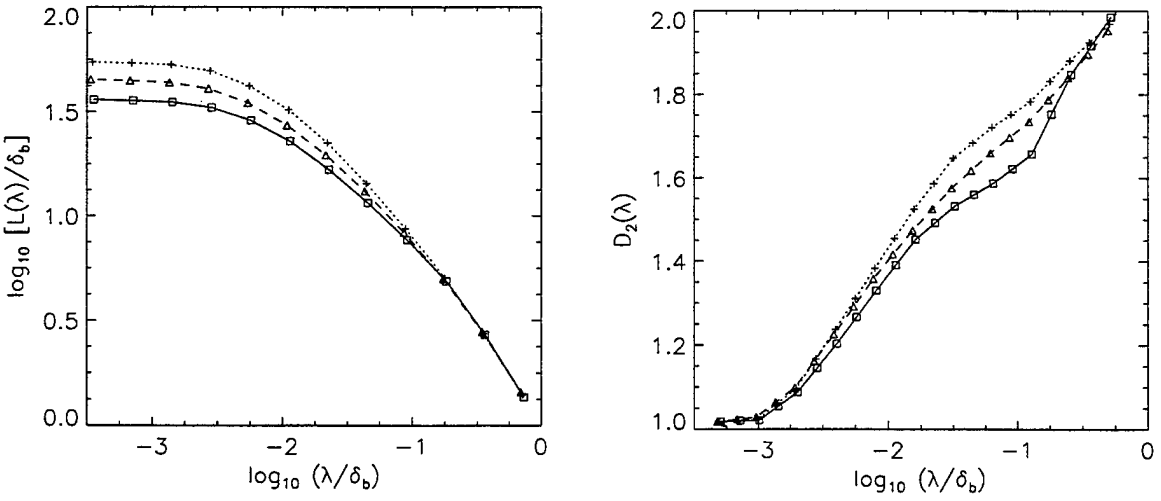

FIG. 14 Coverage length and coverage dimension as a function of (normalized) scale for scalar level sets in a turbulent jet. $Re \simeq 4.5 \times 10^3$: dotted/crosses; $Re \simeq 9.0 \times 10^3$: dashed/triangles; $Re \simeq 18 \times 10^3$: solid/squares.

A new framework was also developed for the study of the geometry of level sets, in general, that extends standard (self-similar) fractal analysis. Relations be-

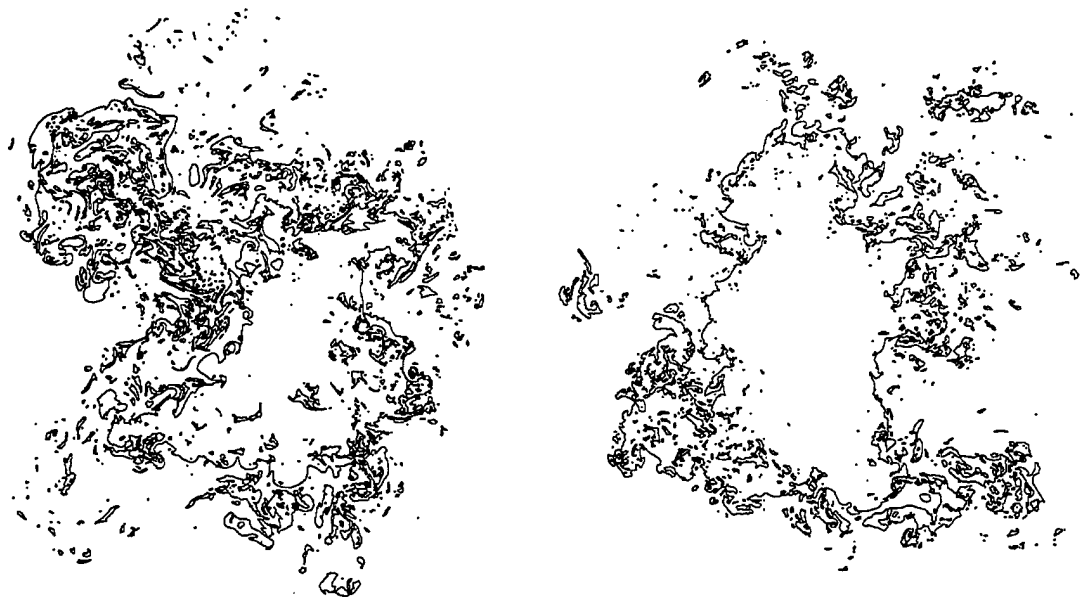

FIG. 15 Scalar c_2 level sets at $Re \simeq 4.5 \times 10^3$ (left) and 18×10^3 (right), indicating simpler topology at higher Reynolds number.

tween coverage statistics and scale distributions, in general, were derived (Catrakis & Dimotakis 1996b). The scale distribution is formulated in terms of a multidimensional (2-D, for these data) spacing scale, defined as the size of the largest empty box (LEB), randomly located in the bounding box of the level set, that contains no part of the level set. At the inner scales, the coverage dimension and LEB-scale distribution were found to be consistent with lognormal statistics. The LEB scale distribution was also shown to provide a dimensionless measure of the surface-volume (perimeter-area, in 2-D) ratio of the level sets, in the small-scale limit. A more detailed description of scale distributions and their relation to (power-law or scale-dependent) fractal geometry can be found in Catrakis & Dimotakis (1996c).

For the jet data, level sets consist of individual (disjoint) "islands" and "lakes", depending on whether the interior is at a lower, or higher, scalar level, respectively. It is useful to analyze island/lake statistics, such as size and shape complexity. In the context of combustion, for example, an island would be associated with an unburnt fuel pocket in a non-premixed turbulent-jet flame. Such an analysis indicates that the size distribution of such features is well approximated by a log-normal pdf, at small-to-intermediate scales (Catrakis & Dimotakis 1996b), as shown in Fig. 16. Size here is defined as $\sqrt{A}$, with A the individual island/lake area.

Returning to chemical reactions and combustion in non-premixed hydrocarbon turbulent flames, in which combustion is largely confined to the instantaneous sto-

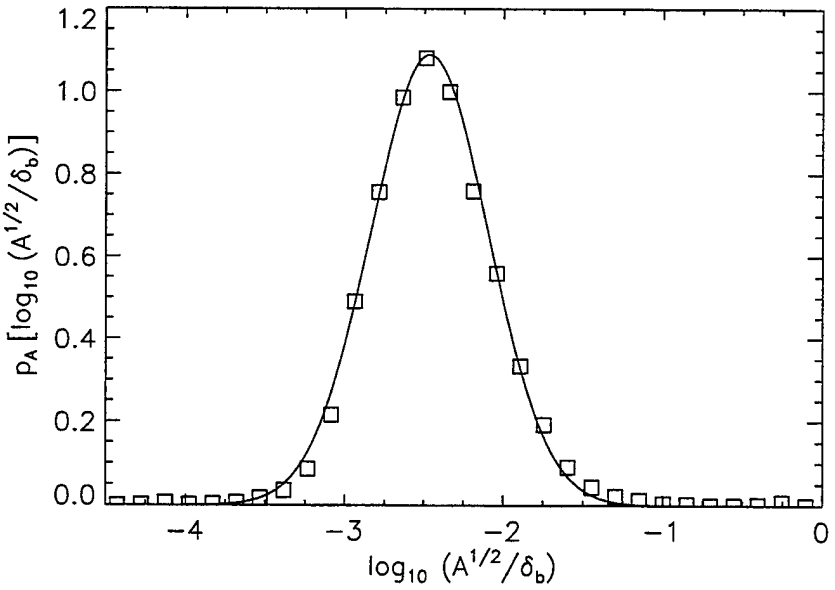

FIG. 16 Size pdf of islands and lakes at $Re \simeq 9 \times 10^3$.

ichiometric (isoscalar) surface (Burke & Schumann 1928), area-volume measures of the isoscalar surface may be used to relate the local burning rate to the time required for the local consumption of unburnt fuel pockets. Such a measure, dubbed *shape complexity*, can be defined as, $1 \leq \Omega_2 \equiv P/[2(\pi A)^{1/2}]$, in 2-D, where P is the perimeter and A the area of an island or lake, with $(\Omega_2)_{\min} = 1$ attained for a circle, and corresponding extensions for Ω_d, for higher-dimensional embedding spaces. The liquid-phase jet data described above indicate that a power law over 3 decades in size (6 decades in area) provides a good approximation for the pdf of shape complexity. This behavior is equivalent to log-Poisson statistics for Ω_2 (Catrakis & Dimotakis 1998).

A coverage analysis was also performed on isodensity data from a Navier-Stokes DNS study of the evolution of a Rayleigh-Taylor-instability flow, of a $Sc \equiv \nu/\mathcal{D} = \infty$ fluid. The flow was initialized with a $\rho = 3$ fluid on top and a $\rho = 1$ fluid on the bottom, in a $256 \times 256 \times 512$ rectangular box. The three-dimensional DNS of the evolving flow was terminated when the spatial-resolution requirements could no longer be met by the fixed grid, at $Re_{\text{final}} \simeq 1.1 \times 10^3$, based on the vertical extent and growth rate of the Rayleigh-Taylor mixing region (Cook 1998). The simulation utilized periodic boundary conditions in the boundary planes transverse to the acceleration vector, and no-slip at the top and bottom faces at the end of the long dimension of the box; aligned with the acceleration vector. A small-amplitude perturbation of the interface between the two fluids initialized the flow.

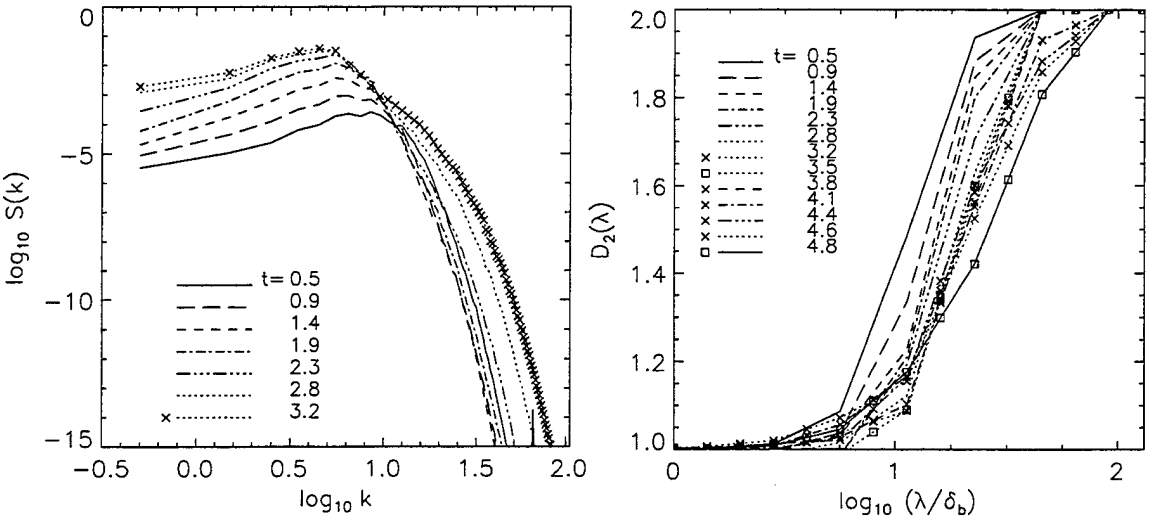

FIG. 17 Temporal evolution of scalar power spectrum (left) and coverage dimension (right) for a 2D slice (at midheight) of the $\rho = 2$ isoscalar surface in a numerical simulation of the Rayleigh-Taylor-instability flow.

As with the jet-flow data, spectral information is not enough to characterize the geometry of isoscalar surfaces. Figure 17 (left) shows the time evolution of the spatial spectrum of the density field in the midheight plane, *i.e.*, of $\rho(x, y, z = 0)$, for the indicated progression in time. The spectrum initially exhibits a temporal progression to lower wavenumbers, a result of diffusive smoothing of the initial density-field perturbation (recall that $Sc = 1$ here). While the low wavenumber spectral content continues to increase, a sustained progression to higher wavenumbers with increasing time (for $t > 1.4$), can be seen, plausibly as the Rayleigh-Taylor and other, secondary, flow instabilities take over, with the spectrum reflecting the growth of small-scale features at the midheight plane.

Figure 17 (right) plots the coverage dimension, $D_2(\lambda)$, for the $\rho(x, y, z = 0) = 2$ isodensity contours, in the same plane, computed by successive binary subdivisions of the midheight slice, as in the jet scalar-data analysis, above. The resulting scale-dependent coverage dimension $D_2(\lambda)$ can be seen to span the range of values from unity (the topological dimension), to 2 (the embedding dimension), smoothly transitioning between the two limiting values, at the smallest and the largest scales, respectively. Interestingly, the temporal progression indicated by $D_2(\lambda)$ is from small to large scales, for $t \lesssim 3.5$, *i.e.*, *opposite* the high-wavenumber trend in the spectral analysis. It is not until near the end of the simulation (for $t \gtrsim 3.5$), where a reversal of this trend is exhibited, at small scales only.

The spectrum measures the wavenumber content of the selected density field, $\rho(x, y, z = 0; t)$, *i.e.*, of the density surface over the midheight (x, y)-plane, while the level-set coverage analysis interrogates the geometry of the $\rho(x, y, z = 0; t) = 2$ contours in the midheight (x, y)-plane, *i.e.*, the slice of the former, at the $\rho = 2$ elevation. The early-time ($t = 0.938$ and 1.875) contours become smoother, while the density surface is developing sharp peaks. The latter are responsible for the spectral progression to higher wavenumbers. This trend continues for a while, with a subsequent transition that can be seen in the behavior of the density surfaces. These develop a more complicated topology, characterized by folds between local maxima and minima, at late times ($t = 4.607$ and 4.810). This also registers in the level-set contours that can be seen to develop small-scale features, on top of the larger-scale features that continue to increase in size.

Viewing the flow evolution through the three-dimensional density-field data (not discussed here) indicates that the likely cause of this transition is the development of secondary instabilities, of the Kelvin-Helmholtz type in the high-shear, near-midheight regions generated by the interpenetrating Rayleigh-Taylor fingers, and the formation of mushroom-like structures at their tips. The cross-over in the coverage dimension, $D_2(\lambda)$, at small scales for late times revealed this transition, even though there is scant, if any, evidence for it in the spectral data. It is an attestation of the scale-local capability of the coverage analysis that such geometrical properties were clearly registered in those statistics. They were subsequently confirmed by computer-visualization of the corresponding field information.

Additional details of this part of the work were presented at the 2$^{\text{nd}}$ *Monte Verita Colloquium on Fundamental Problematic Issues in Turbulence*, 22–28 March 1998 (Ascona, Switzerland) and documented in Dimotakis *et al.* (1998a).

4. Image correlation velocimetry

The brief account below is abstracted from the thesis by Gornowicz (1997), which should be consulted for additional documentation.

The Image Correlation Velocimetry (ICV) method developed as part of work sponsored by this grant, is an extension of the original implementation by Tokumaru & Dimotakis (1995). The new implementation utilizes a hierarchical B-spline representation of the velocity (mapping) field, allowing the desired spatial-continuity

order to be imposed on the solution, as will be discussed below. A very similar approach is used by Szeliski & Shum (1996). These authors also employ a multiresolution-spline representation of the displacement field between image pairs.

The development of the ICV extensions described here, is very similar to the Szelinski & Shum method, that was developed in a different context. Variational methods have been used to infer displacement fields in a variety of contexts, as done by Zhou *et al.* (1995), for example, who employed a multiresolution representation of the three-dimensional displacement field in the interior of a cylindrical asphalt/aggregate core, assuming a volume-preserving (divergence-free) displacement field.

Another general category of this methodology identified by Barron *et al.* (1994) are the so-called differential techniques, pioneered by Horn & Schunck (1981). These methods calculate the components of the scalar-transport equation and use additional constraints to remove ambiguities. Recent work has investigated and compared the required additional constraint(s) to the scalar transport equation proposed by various researchers after Horn & Schunck (*e.g.*, Willick & Yang 1991). Strong proponents of the application of this technique for fluid velocimetry have been Dahm *et al.* (1991, 1992). More recently, a variational approach was offered by Su & Dahm (1995) and Dahm *et al.* (1996). Pearlstein & Carpenter (1995), however, noted that the method of Dahm and collaborators suffers from a local ambiguity problem in that the local velocity field is only defined in the direction of the imaged-scalar gradient. Pearlstein & Carpenter proposed to mitigate this ambiguity problem by simultaneously tracking multiple scalar fields. A shortcoming of these methods is that they rely on spatial and temporal derivatives of the imaged field to deduce the convecting velocity field, rendering them rather susceptible to the inevitable image noise.

4.1 Continuous-field ICV method

The ICV procedure seeks the displacement field, $\boldsymbol{\xi}(\mathbf{x})$, such that the region in the neighborhood of $\mathbf{x}$, in the image $I_1(\mathbf{x})$, at time t_1, is best mapped into the region $\mathbf{x}+\boldsymbol{\xi}$ in the next image, $I_2(\mathbf{x})$, at $t_2 = t_1 + \tau$, *i.e.*, such that,

$$I_1(\mathbf{x}) \mapsto I_2(\mathbf{x}+\boldsymbol{\xi}) \ . \tag{7}$$

Specifically, the displacement field, $\boldsymbol{\xi}(\mathbf{x})$, is sought that minimizes the square of the difference of the two images, integrated over the correlation domain, Ω, *i.e.*, a cost function given by,

$$\mathcal{J}\{\boldsymbol{\xi}\} \;=\; \int_{\Omega} [\, I_2(\mathbf{x}+\boldsymbol{\xi}) - I_1(\mathbf{x})\,]^2 \; \mathrm{d}\Omega(\mathbf{x}) \;\rightarrow\; \min \;. \tag{8}$$

This cost function alone does not guarantee either a unique or smooth solution. Such attributes depend on the functional representation of $\boldsymbol{\xi}$ and are addressed in Gornowicz (1997).

If the time difference, $\tau = t_2 - t_1$, between the two images is small, in some appropriate sense, one can Taylor-expand the displaced-image field at t_2, *i.e.*,

$$I_2(\mathbf{x}+\boldsymbol{\xi}, t_1+\tau) \;=\; I_1(\mathbf{x},t_1) + \tau\,\frac{\partial}{\partial t} I_1(\mathbf{x},t_1) + \boldsymbol{\xi}\cdot\frac{\partial}{\partial \mathbf{x}} I_1(\mathbf{x},t_1) + \;\text{H.O.T.'s}\;.$$

where the higher-order terms are $\mathcal{O}\left(\tau^2\right)$, $\mathcal{O}\left(\boldsymbol{\xi}^2\right)$, or $\mathcal{O}\left(\tau\boldsymbol{\xi}\right)$. A mapping (displacement) field (Eq. 7), *i.e.*, one that produces,

$$I_2\left[\mathbf{x}+\boldsymbol{\xi}(\mathbf{x}), t_1+\tau\right] \;\simeq\; I_1(\mathbf{x},t_1)\;,$$

is seen to be equivalent to the requirement that,

$$\tau\,\frac{\partial}{\partial t} I_1(\mathbf{x},t_1) + \boldsymbol{\xi}\cdot\frac{\partial}{\partial \mathbf{x}} I_1(\mathbf{x},t_1) \;\simeq\; 0\;,$$

again, to leading order in the space/time displacements, *i.e.*,

$$\frac{\partial}{\partial t} I_1 + \mathbf{u}\cdot\frac{\partial}{\partial \mathbf{x}} I_1 \;\simeq\; 0\;, \qquad \text{for,}\quad \mathbf{u} \;=\; \frac{1}{\tau}\,\boldsymbol{\xi}\;. \tag{9a,b}$$

Equation 9 is the optical-flow equation. It is also the scalar-transport equation, provided diffusive effects are negligible, which typically translates to an upper limit on the time interval, τ, between the image pair. Since scalar diffusivity is essentially fixed by the choice of the fluid, the time interval must be chosen such that diffusion is negligible (*cf.* discussion in Tokumaru & Dimotakis 1995).

To compute an optimal mapping field, the ICV method relies on a parametric representation of the displacement field, $\boldsymbol{\xi}(\mathbf{x})$. In several refined DPIV implementations (*e.g.*, Huang 1994, Sholl & Savas 1997), as well as in the previous ICV implementation (Tokumaru & Dimotakis 1995), local Taylor expansions of the displacement field were employed, to various orders, *i.e.*,

$$\begin{aligned}
\boldsymbol{\xi}(\mathbf{x}) \;=\; \boldsymbol{\xi}(\mathbf{x}_\mathrm{c}) \;&+\; (\mathbf{x}-\mathbf{x}_\mathrm{c})_i\,\alpha_{\mathrm{c},i} \\
&+\; \frac{1}{2}\,(\mathbf{x}-\mathbf{x}_\mathrm{c})_i\,(\mathbf{x}-\mathbf{x}_\mathrm{c})_j\,\beta_{\mathrm{c},ij} \\
&+\; \frac{1}{3!}\,(\mathbf{x}-\mathbf{x}_\mathrm{c})_i\,(\mathbf{x}-\mathbf{x}_\mathrm{c})_j\,(\mathbf{x}-\mathbf{x}_\mathrm{c})_k\,\gamma_{\mathrm{c},ijk} \\
&+\; etc.\;,
\end{aligned} \tag{10}$$

where $\mathbf{x}_c$ is any expansion point, with the parameters, $\alpha_{c,i}$, $\beta_{c,ij}$, $\gamma_{c,ijk}$, *etc.*, determined by the DPIV or ICV solution.

In the ICV implementation of Tokumaru & Dimotakis (1995), the minimized cost function included terms which increased its value with the (square of the) amplitude of any discontinuities of the displacement field and its derivatives at the boundaries of the array of Taylor-expansion regions around the selected control points, $\mathbf{x}_c$. As a consequence, much of the built-in flexibility in describing spatial variations of the displacement (velocity) field was lost, with degrees of freedom gained from the Taylor-expansion coefficients in Eq. 10, in effect, expended to minimize discontinuities of the velocity field and of its derivatives at the Taylor-expansion region boundaries.

To mitigate this difficulty, the present ICV implementation relies on a displacement field that possesses the required, $\mathcal{C}^n$, continuity properties by construction, with the order of continuity, n, chosen appropriately, as described below. The remaining (true) degrees of freedom are utilized to minimize the cost function, $\mathcal{J}\{\boldsymbol{\xi}\}$, with no added (smoothing) terms in the integrand.

Velocity- and vorticity-field solutions of the Navier-Stokes equations are continuous, with continuous derivatives to all orders, *i.e.*, are $\mathcal{C}^\infty$. In the present implementation, which was limited to two-dimensional fields, a $\mathcal{C}^2$ displacement (velocity) field was employed, *i.e.*, possessing continuous second derivatives, corresponding to inferred vorticity fields that possessed continuous first derivatives. This was achieved by representing the displacement field in terms of B-splines with appropriate basis functions, whose control parameters, $\mathbf{q}_{ij}^{(r,R)} \in \Re^2$, then provided the parametric description of the displacement field, *i.e.*,

$$\boldsymbol{\xi}(\mathbf{x}) \;=\; \boldsymbol{\xi}\left[\mathbf{x};\, \mathbf{q}_{ij}^{(r,R)}\right] \;. \tag{11}$$

With the solution space of the minimization problem (Eq. 8) restricted in this fashion, the cost *functional*, $\mathcal{J}\{\boldsymbol{\xi}\}$, becomes a *function* of the control parameters, *i.e.*,

$$\mathcal{J}\{\boldsymbol{\xi}\} \;\rightarrow\; \mathcal{J}\left[\mathbf{q}_{ij}^{(r,R)}\right] \;, \tag{12}$$

possessing a minimum where derivatives of $\mathcal{J}$, with respect to each of the $\mathbf{q}_{ij}^{(r,R)}$, vanish. This allows a global minimization over the (selected) image-correlation domain to be sought, using an iterative, multidimensional, conjugate-gradient method over all parameter values, with a suitable initial guess.

4.2 ICV algorithm implementation

The ICV implementation is comprised of a sequence of iterative, algorithmic steps:

- image-data preparation,
- image-correlation domain definition,
- cross-correlation displacement-field initialization, and
- a final, conjugate-gradient displacement-field optimization to minimize the cost function (Eq. 8).

The procedure starts by further processing individual data images, after background removal, illumination normalization, *etc.*, for shot-to-shot intensity variations of the illuminating laser sheet. A geometry file is generated, which specifies the correlation domain, Ω, within the image domain. An initial hierarchy of the B-spline resolution knot grid is specified and any excluded regions from the correlation domain (*e.g.*, laser shadows, imaging occlusions, *etc.*) are also identified. The outer boundary of the correlation domain, Ω, is specified as a polyline (n-sided polygon). Inner boundaries can also be accommodated, allowing correlation domains to be defined that are not simply-connected, as necessary. These boundaries are defined on the first of the two images (for each pair).

The next step initializes the solution at the coarsest resolution level; usually, one spline patch. The initialization is performed by cross-correlating spatially-local windows, using Fourier techniques, as in DPIV analyses (*e.g.*, Adrian 1991, Willert & Gharib 1991). The results of these correlations initialize the mapping vector field, $\boldsymbol{\xi}(\mathbf{x})$. Windows are then centered at the peak of each B-spline basis function and the cross-correlation results are used to determine the corresponding B-spline control parameters, $\mathbf{q}_{ij}^{(r)}$, at the resolution level r.

The initialization, $\boldsymbol{\xi}^{(0)}$, of the B-spline representation for $\boldsymbol{\xi}$, allows Eq. 7 to be applied, producing an initial mapped version of the second image, *i.e.*, $I_2(\mathbf{x}+\boldsymbol{\xi}^{(0)})$, that is "closer" to the first image, $I_1(\mathbf{x})$. Further cross-correlations are run between $I_1(\mathbf{x})$ and $I_2(\mathbf{x}+\boldsymbol{\xi})$ to produce subsequent estimates, $\boldsymbol{\xi}^{(n)}$.

A similar process for determining the displacement field in DPIV, but without FFT's, is outlined in Huang (1994) and termed, "Particle Image Distortion". A fast

version, termed, "Lagrangian Particle Tracking", was introduced by Sholl & Savas (1997). In these implementations, the deduced displacement field was specified in terms of local Taylor expansions, to first and second order, respectively.

The ICV initialization step starts with large cross-correlation windows (up to 256×256 pixels, or $1/4 \times 1/4$ the image domain, for example) to avoid spurious correlations and to pick up any large displacements. This initialization step is particularly important, if there are displacements greater than half the characteristic length of a continuous scalar used to mark the flow (equivalent to a Nyquist criterion). Small-scale features of the velocity field are determined in subsequent stages. This aspect is particularly important, in as much as the subsequent minimization stages may not correct for errors introduced at this stage and a local minimum of $\mathcal{J}(\boldsymbol{\xi})$ might be found instead.

Once large-scale displacements have been found with such windows, the size of the window is successively reduced by a factor of 2, cross-correlations are performed, and the corresponding B-spline parameters are computed to yield the next window-size estimates of the displacement (mapping) field. These successive halvings continue until a user-determined minimum window size is reached.

The displacement field, $\boldsymbol{\xi}$, produced by the cross-correlation sequence is used to initialize an iterative minimization procedure. The projection of the displacement field on the set of B-spline basis functions (*cf.* Eq. 11 and discussion in Gornowicz 1997) converts the integral $\mathcal{J}$ to be minimized from a functional of $\boldsymbol{\xi}$ to a function of the finite number of B-spline control parameters (*cf.* Eq. 12), as noted above. The required minimization of $\mathcal{J}$ is now performed in a finite-dimensional space.

An important part of the ICV implementation is the accommodation of appropriate boundary conditions. The inferred flow fields are typically elliptic, so the choice of appropriate boundary conditions is important. Especially important is the inference of flows in the vicinity of no-slip boundaries, an area that is typically not very well resolved by DPIV-correlation methods.

5. Three-dimensional imaging and visualization

As part of an effort to investigate the three-dimensional structure of scalar fields, a set of three-dimensional, laser-induced fluorescence (LIF) measurements of scalar-species concentration in the far-field of a liquid-phase axisymmetric turbulent jet was undertaken. The spatio-temporal data, consisting of time sequences of LIF images, capture the entire local extent of the jet and are spatially resolved to the diffusion length scale λ_D at $Re \simeq 2.3 \times 10^3$. An in-house designed and constructed digital camera was utilized to record high-resolution (1024×1024), high-dynamic-range (12-bits/pixel) images, acquired at a rate of 10 frames/s.

The space-time structure of the turbulent mixing flow was visualized by reconstructing three-dimensional isoconcentration surfaces from the sequence of LIF images. In collaboration with Dr. David Laidlaw, of the Caltech Biology and Computer Science Department, isosurfaces for a $390 \times 390 \times 4$, 3-D portion of the turbulent jet data were calculated and visualized using the marching-cubes algorithm commonly used in medical imaging (*e.g.*, computed tomography, magnetic resonance, and single-photon-emission computed tomography).

For high Reynolds number turbulence, it is all but impossible to satisfy strict pixel-by-pixel application of the Nyquist sampling criterion. As a result, the conventionally-constructed isoconcentration surface in Fig. 18 is rough, exhibiting steps on the front surface as well as cone-like structures along the left side of the image that are artifacts of temporal aliasing. This aliasing occurs in the standard 3-D isosurface visualization despite the fact that the LIF-image data are temporally resolved with respect to the diffusion-scale advection time $t_\mathcal{D} \simeq \lambda_\mathcal{D}/U$.

Image Correlation Velocimetry (ICV), as described above, extracts velocity information from a succession of images of convected scalars and can be applied to advantage to LIF scalar-field data to facilitate three-dimensional visualization. ICV-derived velocity information is used to generate intermediate interpolated (supersampled) 2-D scalar images that can then be used by standard visualization algorithms to reconstruct the three-dimensional structure of scalar fields.

To satisfy the Nyquist criterion for temporal sampling, ICV was used to construct an additional 19 images in-between each successive frame of LIF data. As discussed above, the displacement field, $\boldsymbol{\xi}(\mathbf{x})$, is represented using bicubic B-splines at a hierarchy of spatial resolutions (*i.e.*, multiresolution) and the minimization of $\mathcal{J}\{\boldsymbol{\xi}(\mathbf{x})\}$ (Eq. 8) is implemented with a multidimensional conjugate-gradient-based

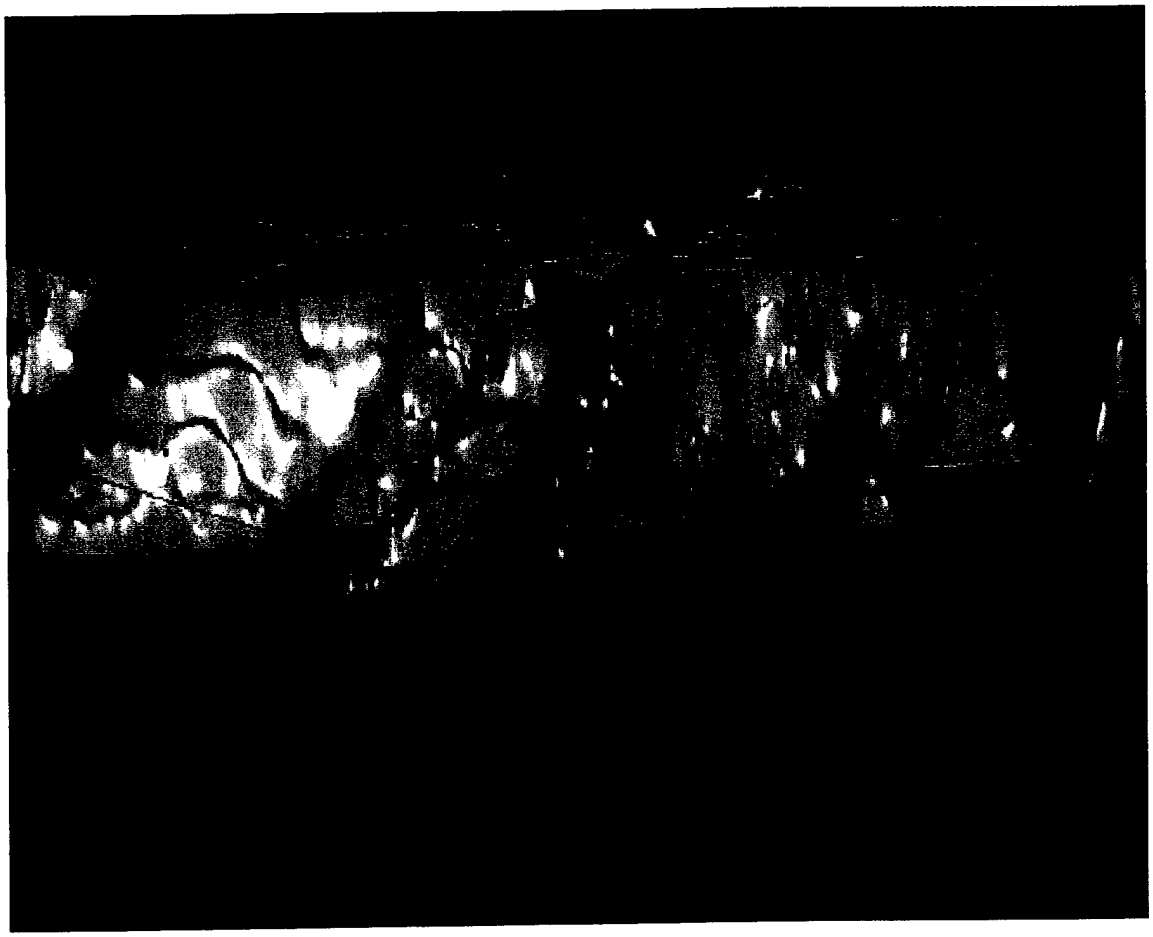

FIG. 18 3-D space-time rendering of scalar isoconcentration surface derived from LIF measurements in the far-field of a turbulent jet at $Re \simeq 2.3 \times 10^3$

approach. With this information, temporally-interpolated images are computed based on the ICV-calculated displacement field, $\boldsymbol{\xi}(\mathbf{x})$, as,

$$I_i(\mathbf{x}) = \frac{1}{2}\left\{ I_1(\mathbf{x} - \alpha\boldsymbol{\xi}) + I_2[\mathbf{x} - (1-\alpha)\boldsymbol{\xi}]\right\} ,$$

where i is an integer, $1 < i < 19$, and $\alpha = i/20$.

Figure 19 depicts an isoconcentration surface computed with the marching-cubes algorithm from the same LIF data as in Fig. 18, using the ICV-interpolated intermediate images. The dealiased (20× supersampled) three-dimensional space-time isosurface is noticeably smoother than the original visualization (Fig. 18). An inclined cylindrical isosurface can be seen along the left edge of the image, rather than two pairs of disconnected "cones". Evidence of developing Kelvin-Helmholtz instabilities can now be seen on the right half of the isoconcentration surface in

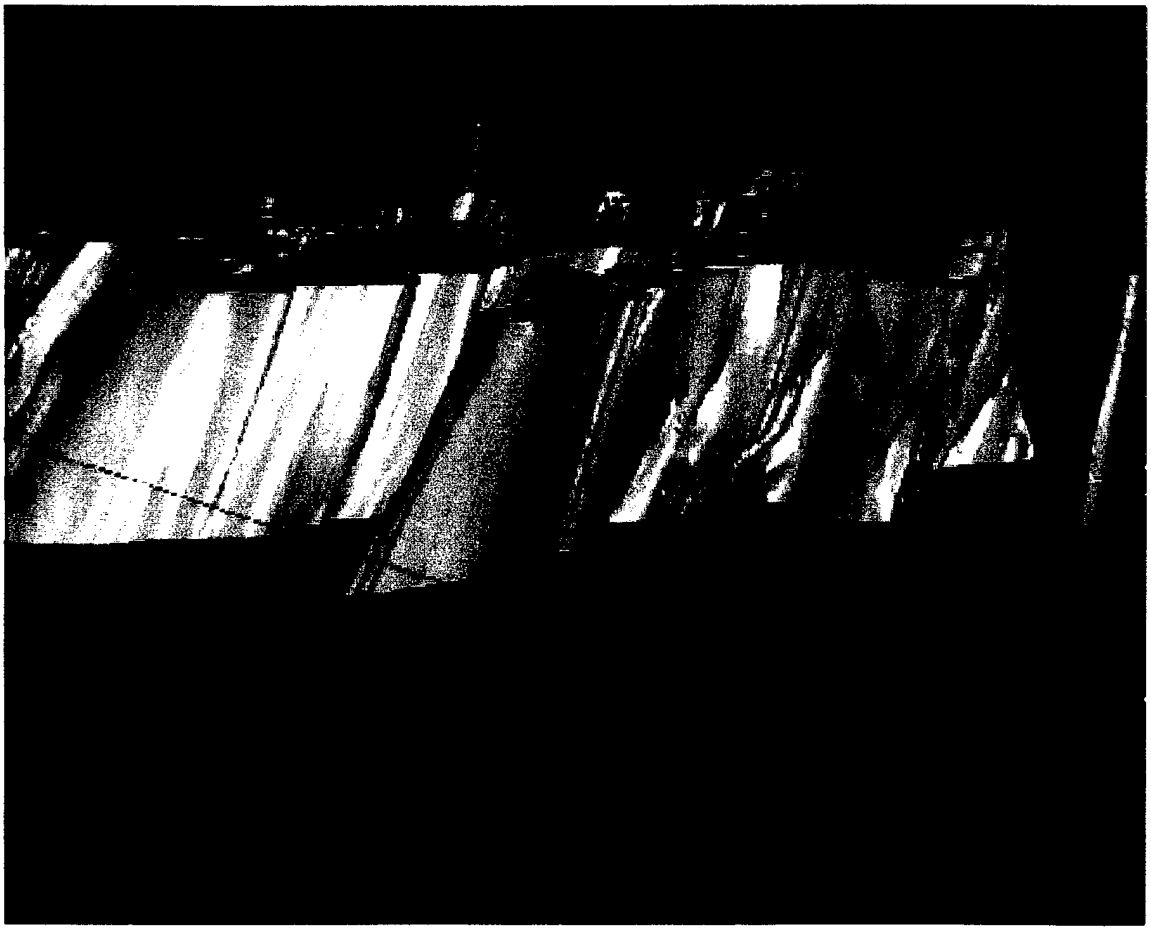

FIG. 19 Dealiased 3-D rendering of scalar isoconcentration surface (same data as in Fig. 18) using Image Correlation Velocimetry to generate intermediate images in time.

Fig. 19. The inverse-slope and orientation of the structure correspond to the local convection velocity of the isoconcentration surface. Our recently-developed technique of incorporating ICV into the isosurface computation has effectively increased the temporal resolution of LIF images of the scalar field.

6. Chemical-kinetic simulations

As described above, the experimental investigations of molecular mixing in subsonic and supersonic turbulent shear layers have relied on $(H_2 + NO)/F_2$ hypergolic mixtures in passive diluents (N_2, Ar, He, *etc.*). This chemical system is hypergolic, with H_2 and NO premixed. On contact, NO and F_2 react spontaneously, producing F radicals, that break the H_2 molecules.

The $(H_2 + NO)/F_2$ system can be kinetically-fast even at modest reactant concentrations and will react to produce a temperature rise that can be directly related to the number of moles of chemical product in the turbulent shear layer (Dimotakis 1991a). In this, high-Damköhler-number limit, the rate of chemical reaction and heat release is limited by the rate of molecular mixing.

Chemically-reacting mixing-layer experiments, such as those described above, indicate that the normalized temperature rise,

$$\theta \equiv \frac{T - T_\infty}{T_f - T_\infty} \ , \tag{13}$$

where T_f is the adiabatic flame temperature and T_∞ the temperature of the unreacted mixture, reaches peak (mean) values in mixing layers in the range,

$$0.45 \lesssim \langle\theta\rangle_{max} \lesssim 0.6 \ , \tag{14}$$

despite the fact that a fraction of the fluid is comprised of (as yet) unmixed reactant freestream fluids (Dimotakis 1991a).. Additionally, the relatively-low concentrations of the $(H_2 + NO)/F_2$ system reactants used in these experiments (and the associated simulations described below) resulted in mixing-limited (high-Da) product formation.

An attempt to model and assess the effect of the detailed chemical kinetics in such experiments was made by Hall & Dimotakis (1987) by considering a simple model in which the chemical reactions were assumed to proceed in a perfectly-stirred reactor. This approach omitted the effects of fluid mechanics (strain rate) and molecular transport.

The present investigation was undertaken to augment the previous studies by conducting a detailed numerical simulation of strained, laminar, opposed-jet reacting flows for the $(H_2 + NO)/F_2$ system, to assess some of the mechanisms affecting the details of the structure and dynamics of the resulting reaction fronts. This flow configuration provides a simple description of the behavior of local diffusion/reaction surfaces, in the turbulent shear zone, that retains the leading-order features of the turbulence-chemistry interactions.

Numerical solutions for a counterflow configuration were obtained using well-established formulations and computer codes (Kee *et al.* 1988, Kee 1991, Kee *et al.* 1985, and Kee *et al.* 1983) . The counterflow code (Kee 1991) was further modified to accommodate non-premixed and premixed reacting modes.

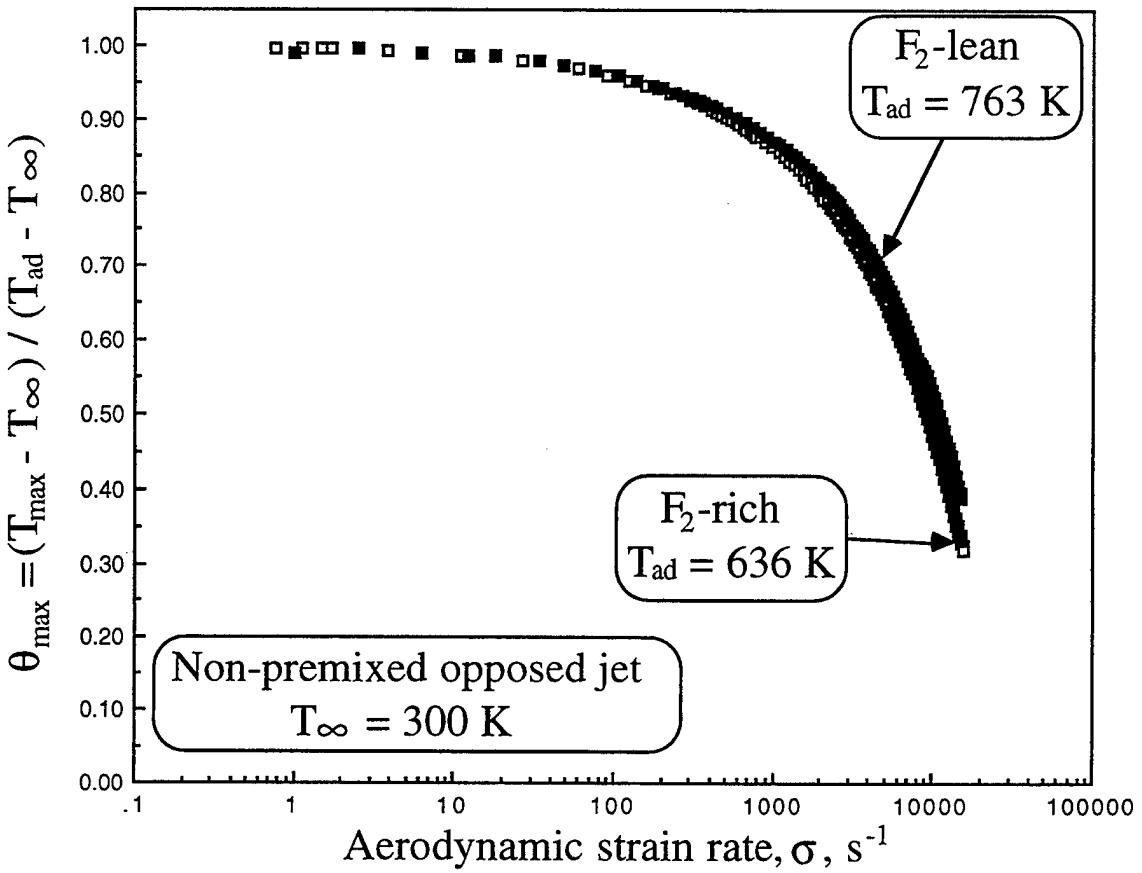

FIG. 20 Effect of aerodynamic strain on maximum temperature, T_{max}, for the non-premixed configuration.

Non-premixed cases were simulated as an impinging F_2/inert-jet onto an opposing $H_2 + NO$/inert-jet stream. Premixed combustion modes were also studied, with identical, opposing $(H_2+NO)/F_2$/inert jets impinging on each other. The premixed mode provides an approximate description of the combustion of premixed reactants fed to the reaction zone as the result of leakage from a neighboring, high-strain-rate diffusion layer; a likely scenario in low-Damköhler number, turbulent-mixing flows. The kinetic scheme includes nine elementary reactions and kinetic parameters (Egolfopoulos *et al.* 1996).

6.1 Non-Premixed Mode

Numerical simulations were conducted for a wide range of strain rates and for nine different reactant cases, defined in terms of reactant concentrations in their respective streams. The molar concentrations were typical of those used in supersonic mixing-layer experimental studies.

As the strain-rate, σ, increases, the maximum temperature, T_{max}, falls, as in high-activation systems; σ was defined as the maximum velocity gradient in the convective zone of the F_2 jet stream. However, turning-point extinction does not occur in such mixtures and, while T_{max} continues to decrease with increasing σ, finite chemical activity persists at strain rates as high as tens of thousands reciprocal seconds. This is illustrated in Fig. 20 for a F_2-rich and a F_2-lean reacting configuration, in terms of the variation of the normalized temperature rise, θ (Eq. 13), with σ. In these simulations, T_∞ was 300 K, with T_f computed from equilibrium calculations using the STANJAN program (Reynolds 1986).

The mechanisms responsible for the temperature reduction with increasing strain rate (*cf.* Fig. 20) were also studied. Reaction-path analyses confirmed that the reaction,

$$NO + F_2 = NFO + F \qquad \text{(R1)}$$

is responsible for the chain initiation by releasing an F atom. This is used by reaction,

$$F + H_2 = HF + H \qquad \text{(R4)}$$

for H_2 consumption and the production of the final HF product and active H radicals. The H radicals then react with F_2, through

$$H + F_2 = HF + F\ , \qquad \text{(R3)}$$

to produce HF and F, which is further used in R4.

The reactant-leakage mechanism is traceable to the finite kinetic rate. Characteristic time scales for the destruction of NO, F_2, and H_2 at the location of the maximum rate of R1, R3, and R4, respectively, were determined and scaled by the strain rate, σ, to form Damköhler numbers for all three species. The results are shown in Fig. 21, for both the F_2-rich and F_2-lean cases. It can be seen that *Da*'s decrease with σ and attain values of order unity at high strain rates. For both F_2-rich and -lean cases, the *Da* of F_2 have lower values compared to NO and H_2. This indicates that the main leakage mechanism is that of F_2, through R3.

These observations were further supported by detailed sensitivity analyses, in which the effect of individual elementary reactions on T_{max} was determined at different strain rates. Representative results are shown in Fig. 22, for the F_2-rich and F_2-lean cases. For both cases, R1, R3, and R4 favor T_{max}, with R3 having the highest positive sensitivity. Furthermore, both cases confirm that R1 is very important, initiating the reaction between the two main reactants, NO and F_2. As expected, negative sensitivity on T_{max} is exhibited by the three-body recombination reactions.

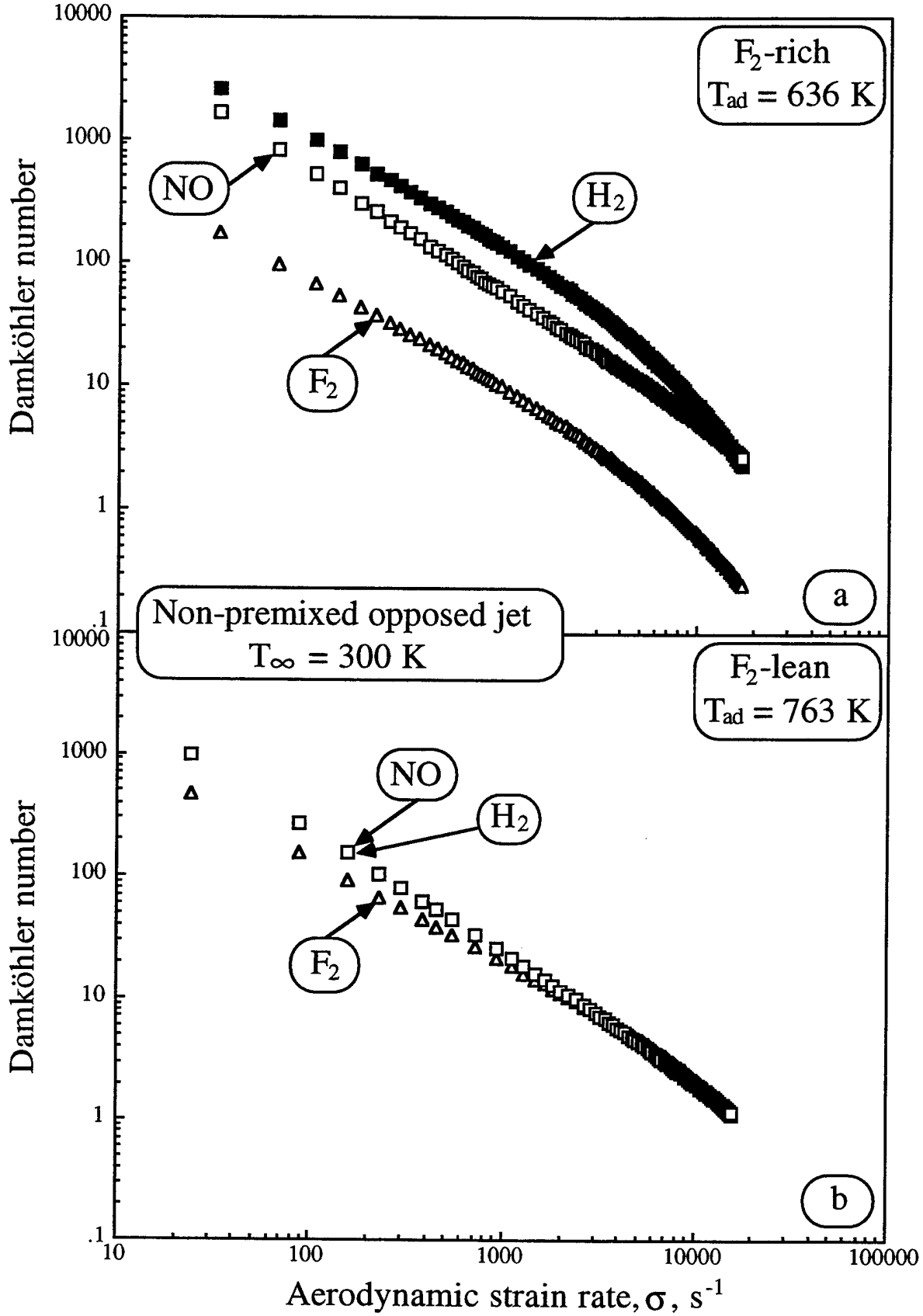

FIG. 21 Damköhler numbers, based on minimum reaction time of various species as a function of imposed strain rate. Top: F_2-rich, bottom: F_2-lean.

6.2 Premixed Mode

For all nine non-premixed configurations and for strain rates of the order of 10^4/s, or so, which are of the order encountered in supersonic mixing-layer experiments, $T_{\max}$ is substantially reduced (Egolfopoulos *et al.* 1996). This indicates reduced chemical activity and that unreacted species will mix and react, within highly-strained flow structures, in a premixed mode. To study this scenario, various configurations of premixed reaction in strained flow fields were investigated. For those studies, the composition of the premixed species was determined using a value of the (molar) entrainment ratio, between the high-speed and low-speed stream (Dimotakis 1991b), of $E_n = 1.06$ (Hall *et al.*1991 and Bond & Dimotakis 1993).

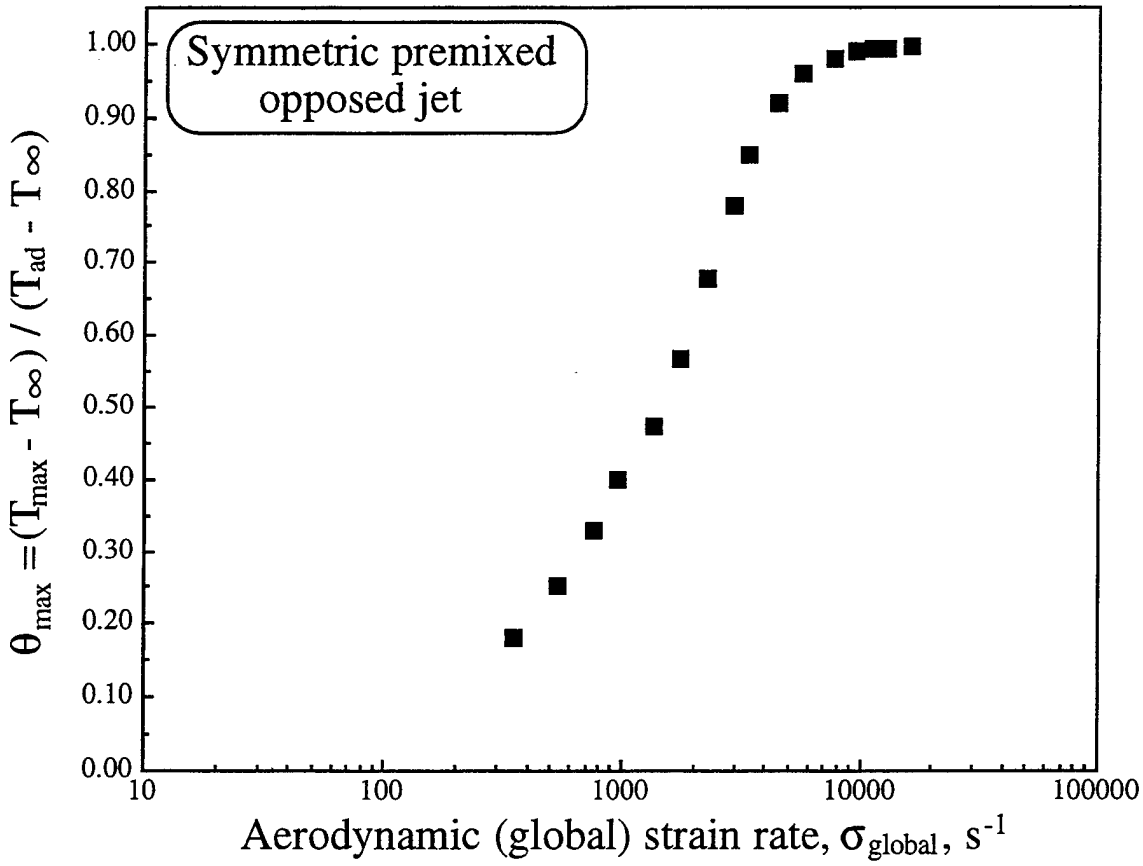

FIG. 23 Effect of aerodynamic strain rate on maximum temperature, $T_{\max}$, for the premixed configuration.

Two identical premixed jets impinging onto each other were studied. As a consequence of this implementation, for low strain rates, losses resulting from high

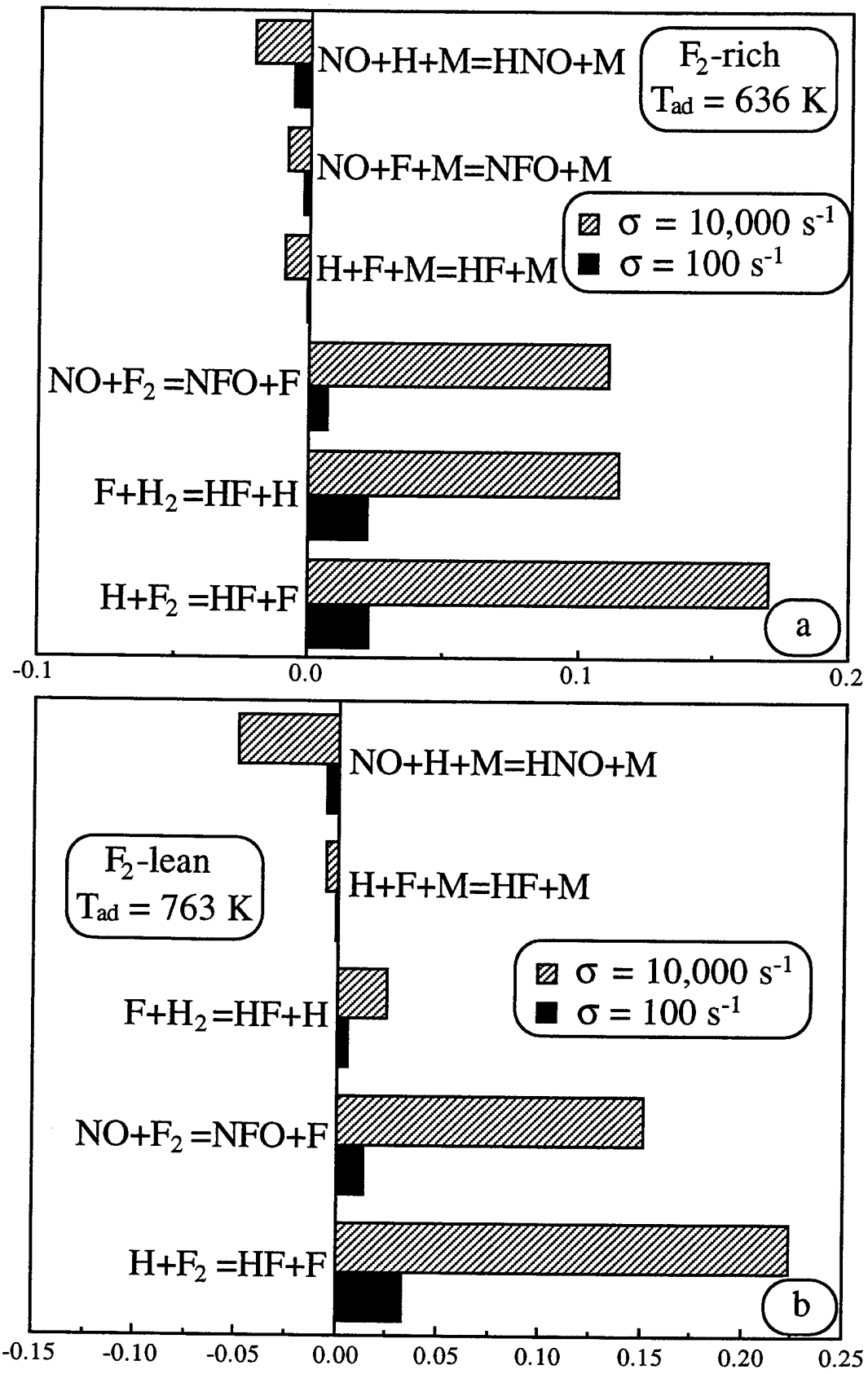

FIG. 22 Normalized sensitivity coefficients at low and high strain rates. Top: F_2-rich, bottom: F_2-lean.

temperature gradients at the nozzle exit result in T_{max} well below T_f. As the strain rate increases, temperature gradients at the nozzle exit decrease, decreasing boundary losses, and T_{max} approaches T_f, corresponding to homogeneously-mixed reactants (*cf.* Fig. 23). In the premixed mode simulations, the convective transport was measured by a global strain rate, σ_g, defined as the nozzle-exit velocity, divided by half the distance between the two nozzles. For all other cases studied, the response of T_{max} to the imposed strain rate was found to be similar.

The asymptotic behavior for high strain rates, *i.e.*, $T_{max} \rightarrow T_f$, is at variance with typical, high-activation, premixed combustion, in which the combination of preferential diffusion and the strain-rate field leads to T_{max} well above, or below, T_f. This difference is clearly attributable to the hypergolic nature of the reacting system. Detailed reactant-flux analysis revealed that the ability to establish strain rates well above values encountered in the combustion of typical fuels can result in convective fluxes that are substantially larger than diffusive fluxes, everywhere. Thus, convection is the dominant transport mechanism with all properties transported at the same rate, leading to a "locally-conserved" system.

The results summarized in Fig. 20 indicate that only a negligible fraction of the normalized temperature rise, θ, can be expected to be contributed by combustion in non-premixed strained diffusion-flame regions, at strain rates of order 15,000/s, and greater. Yet, such, and substantially greater, values for the strain rate are expected in the high-speed, chemically-reacting shear layers discussed earlier. In particular, the amount of chemical product measured in these flows is not reconcilable with the predicted chemical product formation in strained-flame regions in these simulations, considering the strain-rate values these flows can sustain. We are forced to conclude that the preponderant fraction of chemical-product formation, in these flows, occurs in the premixed mode, or, equivalently, a negligible volume fraction of mixed fluid can be found in non-premixed, strained diffusion layers. Where such layers do occur, the conditions for this combustion mode will be created as a result of the substantial reactant leakage, predicted to emanate from high strain-rate diffusion-flame regions in the present simulations. Combustion in this mode can provide the only candidate mechanism to explain the high attained values of the normalized temperature rise observed experimentally (Eq. 14).

Additional details of this part of the work were documented in Egolfopoulos, Dimotakis, and Bond (1996).

7. Numerical simulation of flows with strong fronts

Work on the numerical simulation of flows with strong fronts continued, based on the ideas and simulation technology in terms of Riemann Invariant Manifolds (Lappas 1993, developed under a previous AFOSR grant, Lappas *et al.* 1993, and Lappas *et al.* 1998). In particular, under sponsorship of this Grant, this numerical-simulation methodology was extended to flow systems with source terms in the equations of motion, as occur in chemically-reacting systems (Papalexandris 1997), for example. The new developments permitted the reliable simulation of unstable (underdriven) one-dimensional detonation phenomena, using a Zeldovich-von Neuman-Doering, one-step chemical-reaction (ZND) detonation model (Papalexandris *et al.* 1997a), and, more recently, the extension to two-dimensional detonations (Papalexandris *et al.* 1997b).

A key element in these developments has been the extension of the classical theory of characteristics permitting the numerical simulation of various strong-front phenomena without resorting to operator dimensional- as well as flow/chemistry-operator splitting. By way of example, this permitted the simulation of one- and two-dimensional detonation phenomena with a general, maathematically-consistent set of equations, without resorting to added numerical viscosity or other numerical-dissipation artifices.

The discussion below describes the application of this methodology to unsteady detonation fronts over wedge geometries in hypersonic flow.

7.1 Numerical study of wedge-induced detonations

In this section, numerical simulations of wedge-induced detonations, using the proposed unsplit scheme, are presented. The wedge is placed instantly in uniform flow of a reactive gas. A shock forms immediately at the wedge. If the surrounding gas were inert, this shock would be oblique, at an angle that is prescribed with respect to the centerline of the wedge. However, because the gas is reactive, the shock is curved due to dilatation of the reacting material behind the shock. In particular, a detonation wave can be established downstream, if the shock temperature is high enough.

The wedge angle, θ, is an important parameter in this problem. It is expected that for small wedge angles the shock turns smoothly and the flow far downstream

consists of an oblique ZND wave, *i.e.*, a ZND wave with a non-zero transverse velocity component. For small wedge angles, both the inert and equilibrium shock-polars admit solutions for the shock angle, β. The shock near the tip is essentially inert and its angle can be computed from the inert shock-polar. The angle of the ZND wave, far downstream, can be computed from the equilibrium shock-polar. Given the state ahead of the shock, denoted by the subscript "1", one can determine the flow variables behind the shock, denoted by the subscript "s", by employing the standard kinematic relations for oblique shocks:

$$F \equiv \frac{1+\gamma M_{1n} \pm \sqrt{(M_{1n}^2-1)^2 - 2(\gamma+1)M_{1n}^2\, q_0/(c_p T_1)}}{(\gamma+1)M_{1n}^2}\,, \tag{15a}$$

$$\frac{\rho_1}{\rho_s} = F = \frac{\tan(\beta-\theta)}{\tan\beta}\,, \tag{15b}$$

$$p_s = p_1 + u_1^2\,(1-F)\,\sin^2\beta\,, \tag{15c}$$

where M_{1n} is the normal Mach number ahead of the shock:

$$M_{1n} \equiv \frac{u_1 \sin\beta}{\sqrt{\gamma T}}\,. \tag{16}$$

For wedge angles larger than a certain value (but small enough so that the equilibrium shock-polar admits a solution for β), the shock cannot turn smoothly, and a strong explosion is expected to occur on the front. This explosion is caused by the interaction of pressure waves inside the reaction zone. These pressure waves are emitted from the points at which the material near the wedge burns rapidly due to thermal runaway.

7.2 Detonation induced by long wedges

Three different cases have been examined numerically. Schematic of the geometrical configuration and the computational domain is given in Fig. 24. The wedge is assumed to be long so that the wedge corner has no effect on the flow-field near the reaction zone. Inflow conditions have been assigned at the left boundary and at the first 7 cells of the bottom boundary. Reflecting conditions have been assigned at the rest of the bottom boundary, and outflow conditions have been assumed at the top and right boundaries. The flow at these boundaries is supersonic, and one must ensure that all information for the evaluation of the boundary fluxes comes from inside the domain. This is achieved by copying boundary-cell values to their corresponding dummy cells.

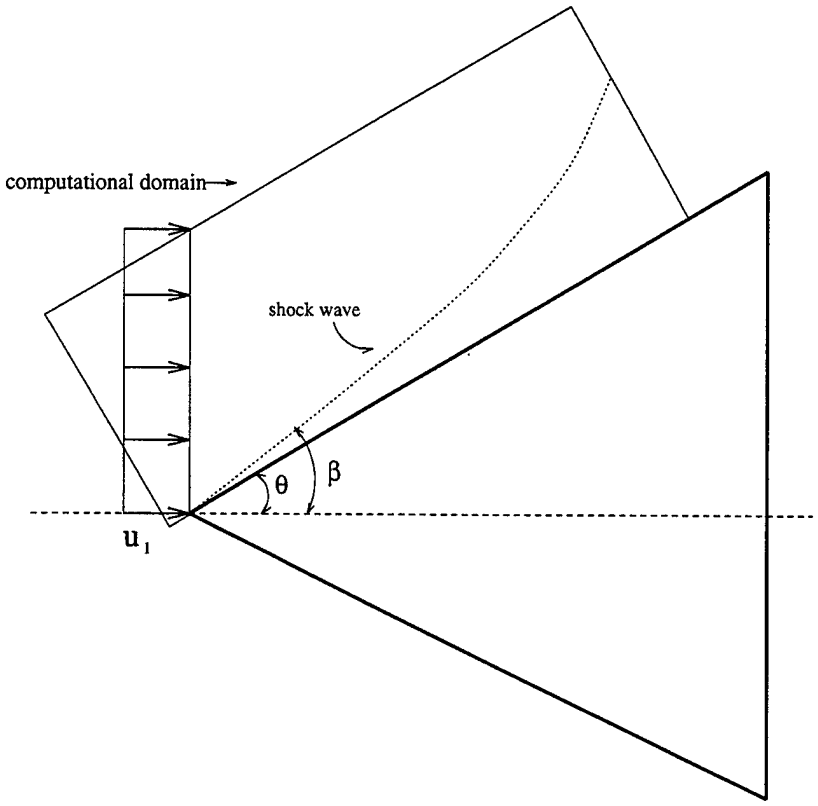

FIG. 24 Schematic of the computational domain for the problem of a detonation induced by a long wedge.

The values of the specific heat ratio, γ, and the heat-release coefficient, q_0, are set as follows:

$$\gamma = 1.2\,, \qquad q_0 = 50\,.$$

Upstream, the pressure and density of the gas are set to unity. All the variables and parameters of the system of equations have been made dimensionless with respect to this upstream state. The results of the simulations are plotted with the same format that was used in the previous section, *i.e.*, contour plots of the pressure, temperature, vorticity, and reactant mass fraction are presented. Each plot consists of 30 contours, equally distributed between the extremal values, except for the plots of the reactant mass fraction, which contain 11 contours, at the levels $z = 0.01\,, 0.1\,, 0.2, \ldots,$ 0.9, 0.99. In these simulations, the Courant-Friedrichs-Lewy (*CFL*) number, $U\,\Delta t/\Delta x$, where U is the flow speed, and Δx and Δt are the magnitudes of the spatial and temporal increments, is set to 0.70.

Case A

This is a low activation-energy case, *i.e.*,

$$E_a = 10 , \qquad K = 3.1245 .$$

As a first test, the wedge angle is set to $\theta = 20°$. The upstream velocity of the gas is $u_1 = 12.171$. Given these parameters and upstream conditions, the theoretical prediction is that far downstream this detonation reduces to an oblique ZND wave of overdrive factor $f = 1.2$ and at an angle $\beta = 34.02°$. The equivalent channel-flow problem was examined in the previous section (case E).

The computational domain is resolved in 960×400 cells. This resolution results (nominally) in 8 points per half-reaction length, *i.e.*, the distance required for half the chemical reaction to be completed locally, for the steady (ZND) solution. In this simulation, the shock wave turns smoothly until it reaches the asymptotic angle. Contour plots for this case are presented in Fig. 25a. These plots are taken at $t = 24.0$. No change in the flow variables is observed at later times, which implies that the part of the flow-field that is covered by the computational domain reaches a steady state.

In the area near the tip of the wedge, no chemical reactions have had the chance to occur and the shock is essentially inert. The pressure and particle velocity in this region are almost constant along a streamline, and chemical reactions take place due to the phenomenon of thermal runaway. The temperature increase across the oblique shock is small, and, consequently, the source term in the species equation remains too small to initiate a rapid reaction. This source term, however, is not zero, so the material does burn, if very slowly.

The region of slow burning is the induction zone. At the end of the induction zone, the temperature has risen high enough to initiate and sustain fast burning of the gas. As a result of the fast burning of the material near the wedge, pressure waves are transmitted to the shock front. These waves interact with the slow-burning region behind the shock, causing fluid elements to burn faster and dilate, and the shock front to turn. Recall that the phenomenon of thermal runaway was also encountered in the study of one-dimensional detonations near the Chapman-Jouguet (C-J) point. This thermal-runaway mechanism is responsible for the formation of pockets of unreacted material in such flows, as discussed in Papalexandris (1997).

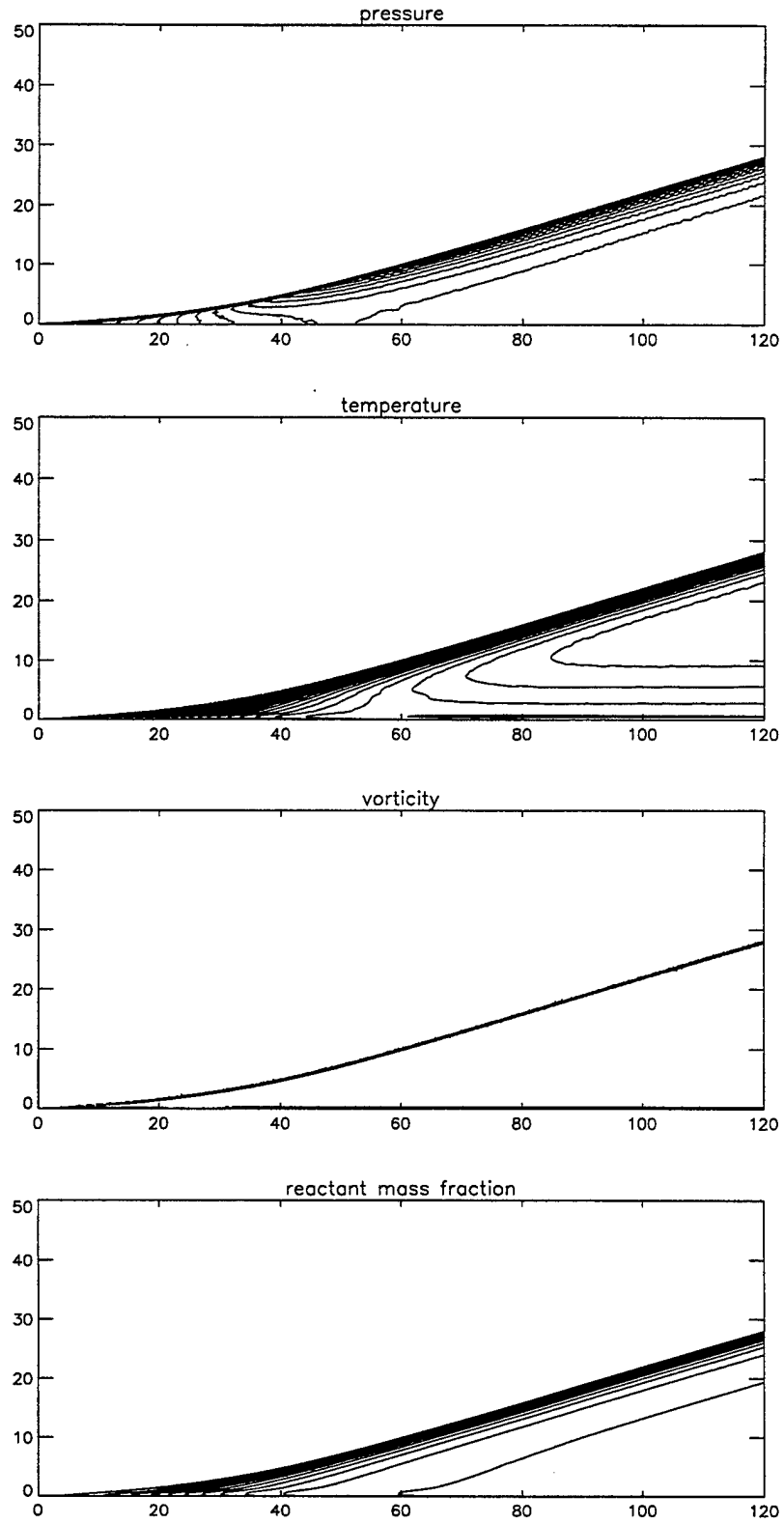

FIG. 25a Case A, $\theta = 20°$: contour plots of the flow variables at $t = 24.0$.

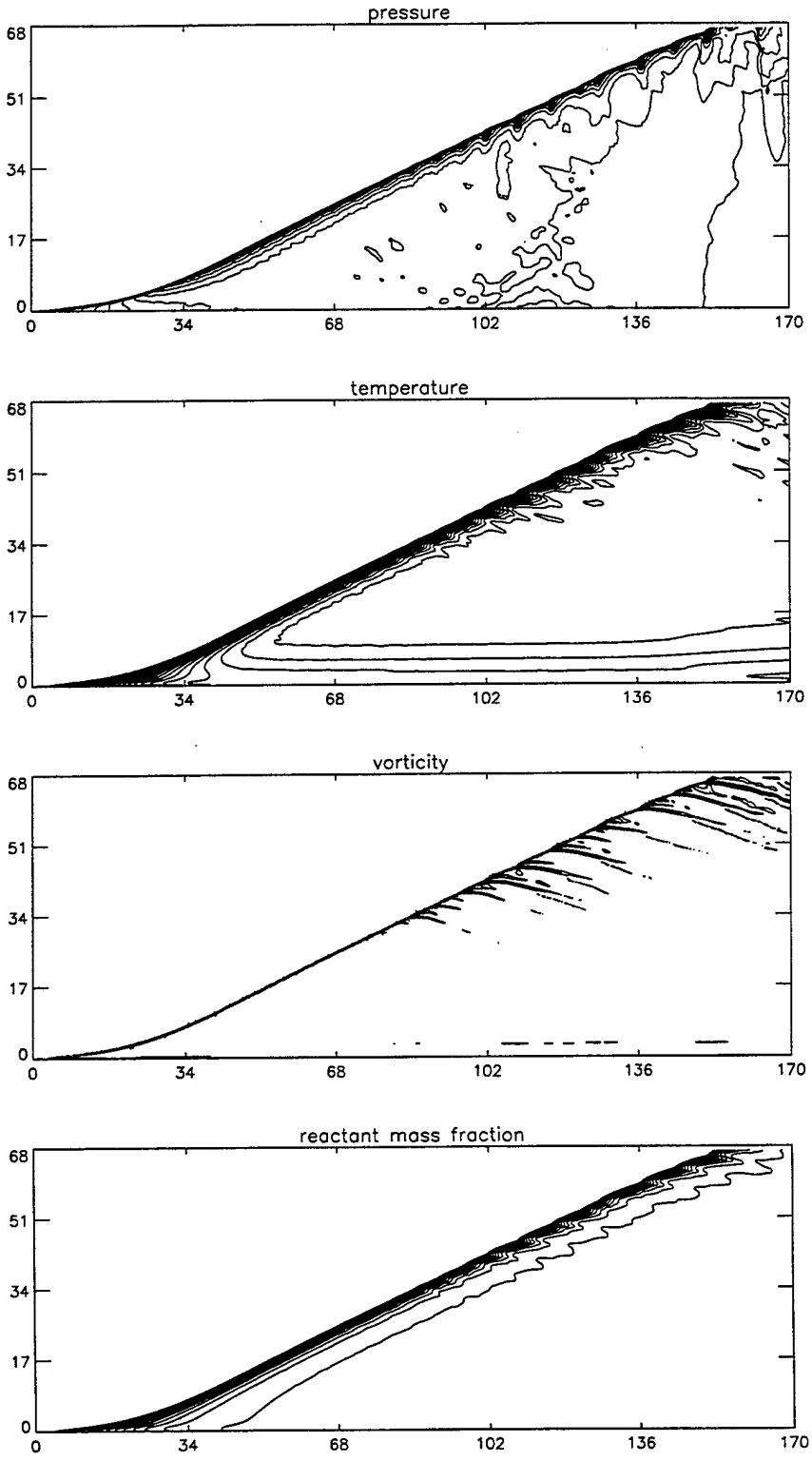

FIG. 25b Case A, $\theta = 27°$: contour plots of the flow variables at $t = 50.0$.

Next, the wedge angle is increased to $\theta = 27°$. This is the maximum angle for which the equilibrium shock-polar admits a solution for β. For a detonation with an overdrive factor $f = 1.2$ to occur, the upstream velocity has to be $u_1 = 9.255$. The asymptotic limit of the shock angle is readily found to be $\beta = 53.7°$. The computational domain for this simulation consists of 1020×402 cells, yielding a nominal resolution of 6 points per half-reaction length. Contour plots of the variables for this problem, at $t = 50.0$, are given in Fig. 25b. In these plots, several triple points can be seen to have formed along the leading front. These triple points move with different velocities. Therefore, collisions between the triple points will eventually occur (most likely outside the area covered by the computational mesh), forming the well-known cellular structures behind detonation waves. Formation of triple points should have been observed in the previous simulation (when $\theta = 20°$), had the computational domain been large enough.

Case B

The activation energy and the stiffness coefficients are now set at:

$$E_a = 50 , \qquad K = 99.762 .$$

The wedge angle is $\theta = 20°$. The upstream velocity is $u_1 = 20.58$. Theoretically, the shock angle should tend asymptotically to $\beta = 27.9°$. In this limit, the detonation is an oblique ZND wave with an overdrive factor of $f = 2.0$.

Three different resolutions have been used for this problem. In the first test, the computational domain consists of 285×60 cells (Fig. 26a). In the second test, it consists of 570×120 cells (Fig. 26b). In the final test, it consists of 1140×240 cells (Fig. 26c), corresponding to a nominal resolution of 6 points per half-reaction length of the one-dimensional, steady-state solution. Again, the shock turns smoothly until it reaches a steady state, very close to the asymptotic limit.

The results presented in Figs. 26 are taken at $t = 18.0$. By this time, the solution has already reached the steady state. It is expected, however, that formation of triple points occurs further downstream. Unfortunately, the current constraints on computational resources did not allow a large-enough domain to be implemented so as to include the region where triple-points occur. The same steady-state solution has been computed with all three meshes. As expected, the shock profiles on the coarse meshes are more smeared than the ones on the fine mesh.

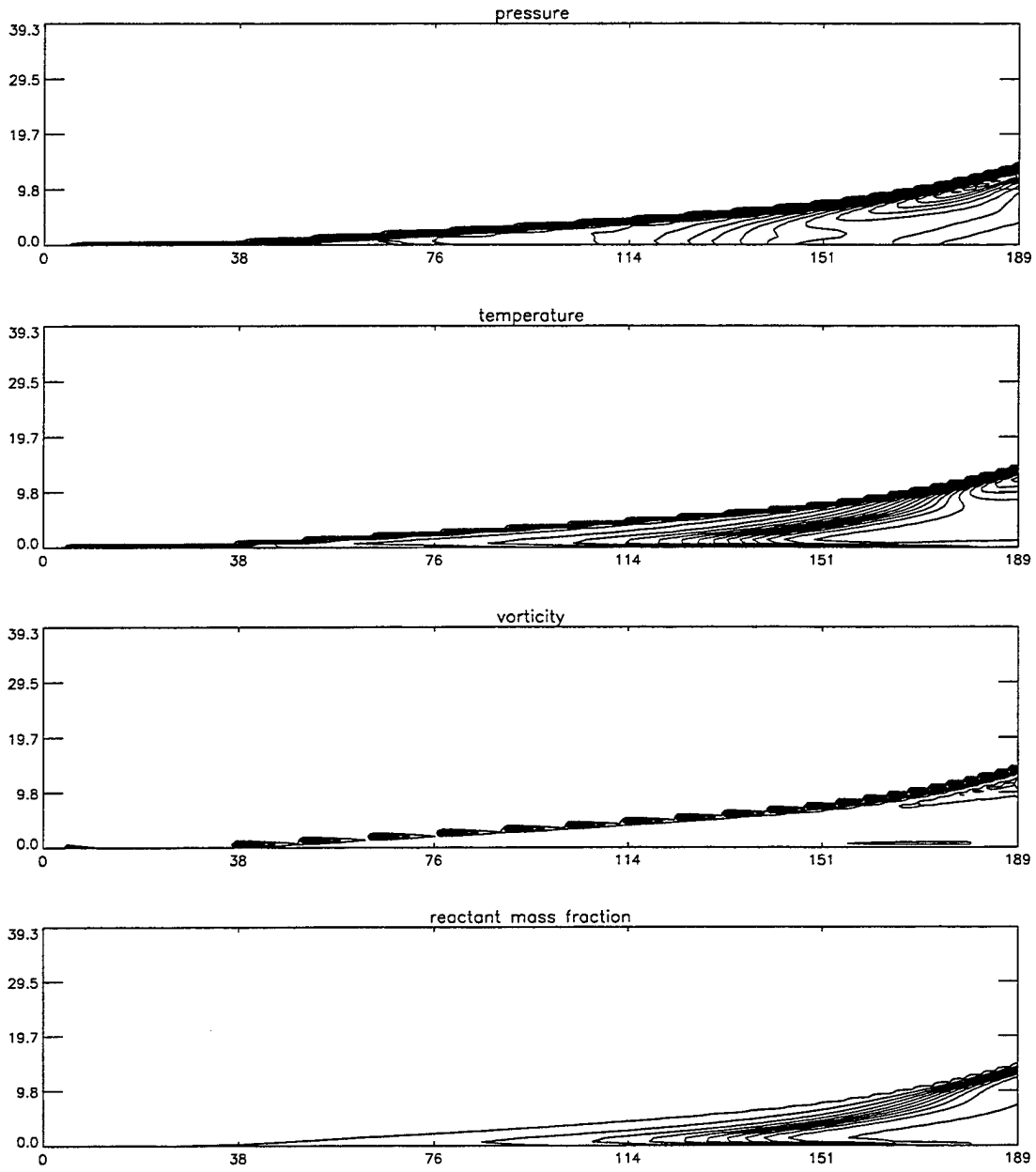

FIG. 26a Case B, $\theta = 20°$: contour plots of the flow variables at $t = 18.0$. Resolution, 285×60 cells.

Next, the wedge angle is increased to $\theta = 35°$, which is near the maximum angle for which the equilibrium shock-polar admits a solution. As before, three different mesh sizes have been used for this problem, consisting of 560×64 cells, 560×128 cells, and 1140×240 cells, respectively. The finer computational domain corresponds

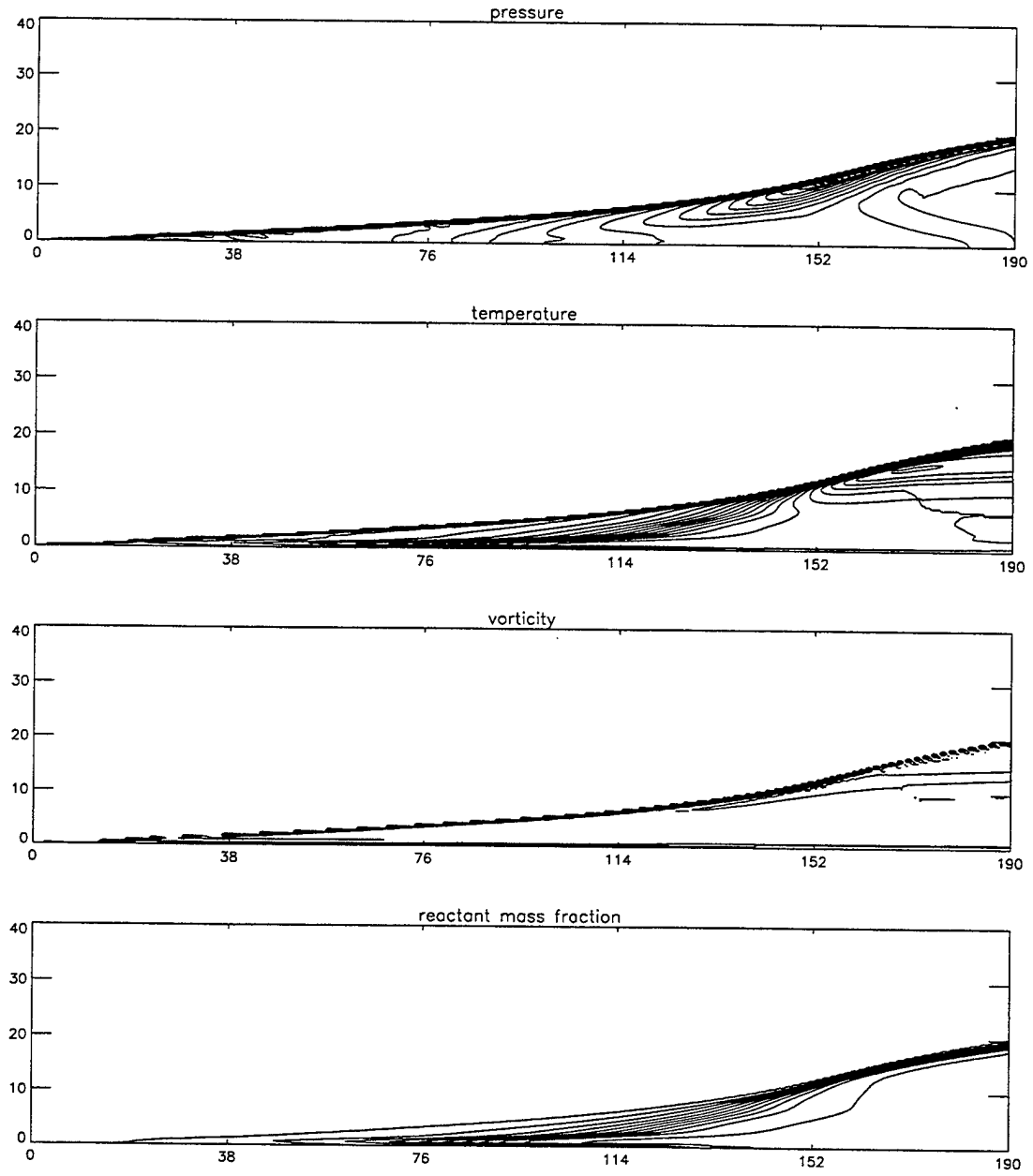

FIG. 26b Case B, $\theta = 20°$: contour plots of the flow variables at $t = 18.0$. Resolution, 570×120 cells.

to a nominal resolution of 8 points per half-reaction length. The upstream velocity is $u_1 = 11.509$. The asymptotic limit is a detonation with an overdrive factor of $f = 1.2$ and at an angle of $\beta = 56.8°$. Results for this simulation, at $t = 50.0$, are given in Figs. 26d, 26e, and 26f. The flow cannot turn smoothly in this case,

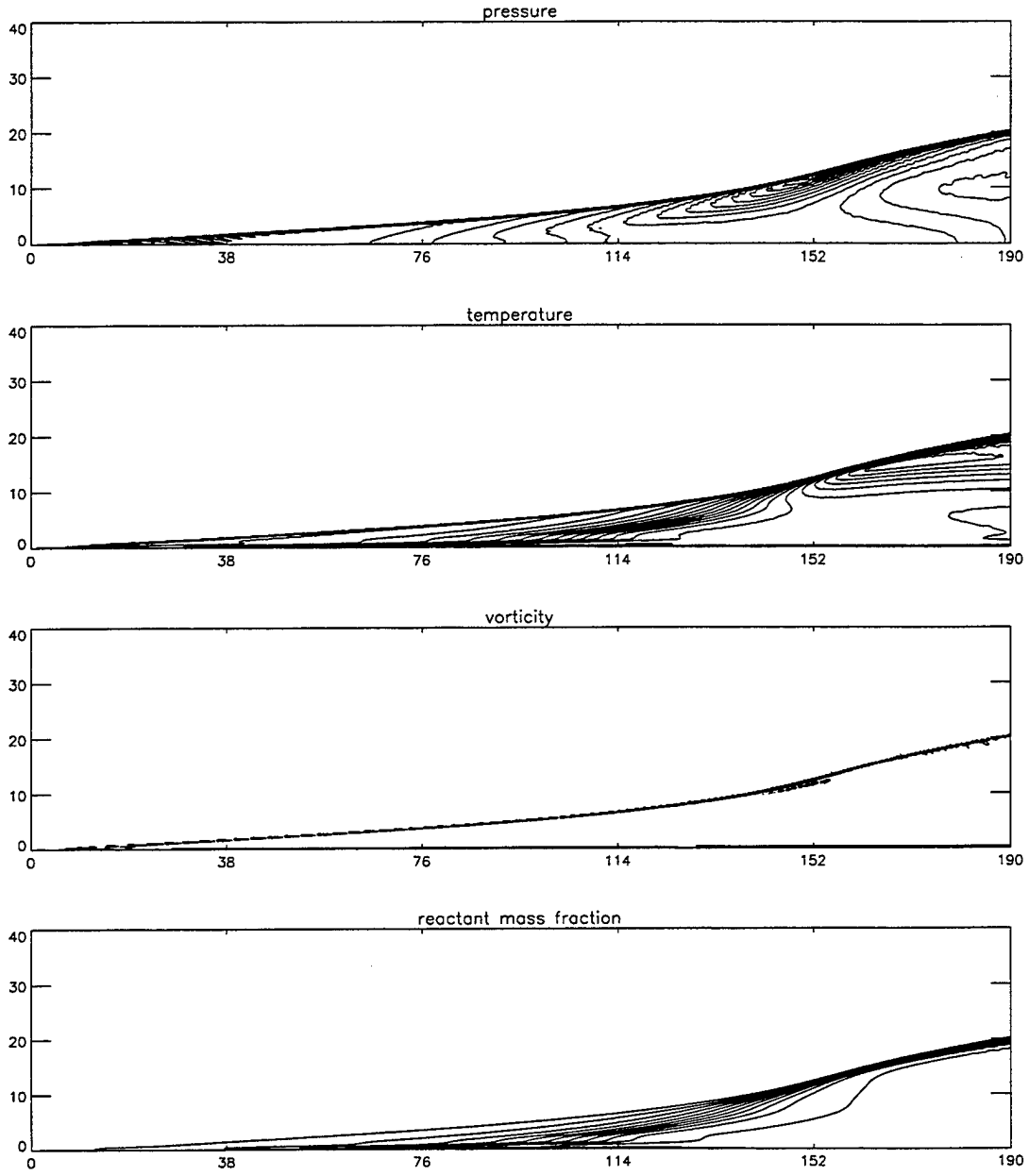

FIG. 26c Case B, $\theta = 20°$: contour plots of the flow variables at $t = 18.0$. Resolution: 1140×240 cells.

because of the high value of the wedge angle.

As a result, a strong explosion takes place at the front. The center of the explosion is a triple point. The incident shock and the Mach stem are the two

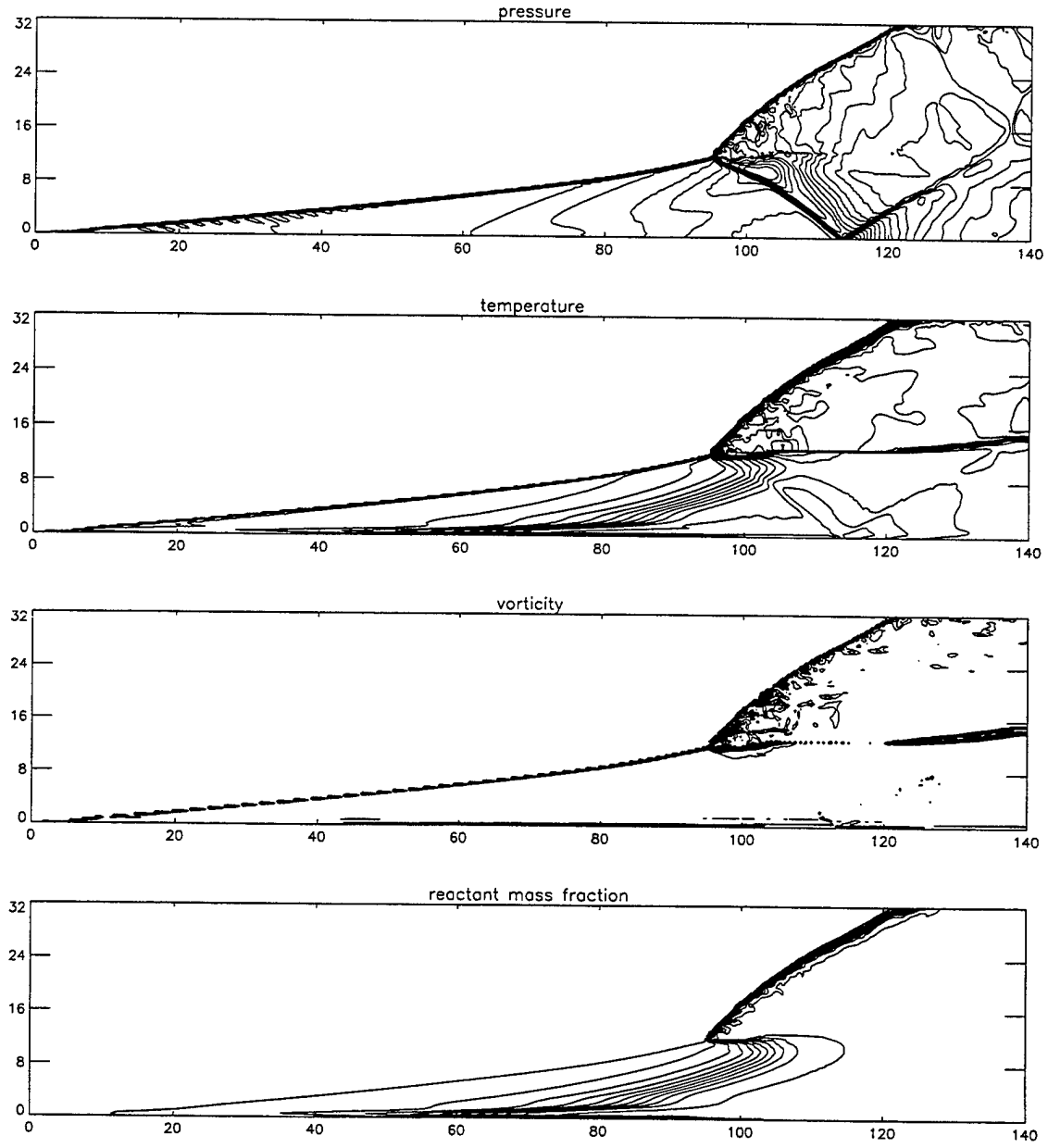

FIG. 26e Case B, $\theta = 35°$: contour plots of the flow variables at $t = 50.0$. Resolution, 560×128 cells.

parts of the main front, below and above the triple point, respectively. Another (reflected) shock emanates from the triple point, which hits the wedge and reflects back. Additionally, a contact discontinuity (shear layer) is formed between the Mach stem and the reflected shock. The material behind the incident shock burns

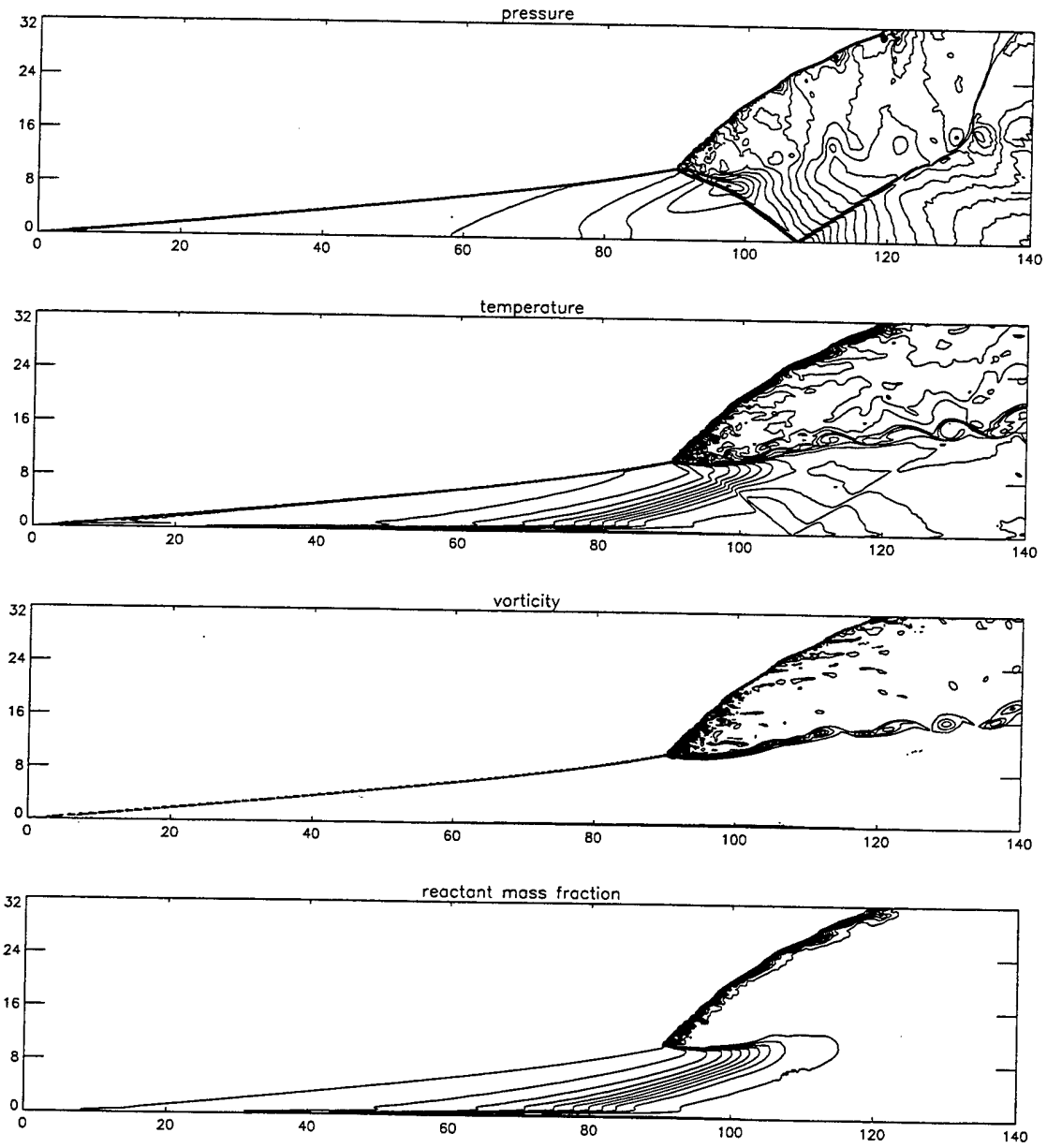

FIG. 26f Case B, $\theta = 35°$: contour plots of the flow variables at $t = 50.0$. Resolution, 1120×256 cells.

due to thermal runaway, but the material behind the Mach stem burns fast because of the high temperature rise due to the explosion. Consequently, there are strong density and temperature gradients across the shear layer. The shear layer becomes unstable very quickly and generates strong vortical structures that are convected

downstream, as seen in Fig. 26f. Diffusion in these simulations is introduced by the discretization of the equations and the truncation error of the scheme. Consequently, the size and the velocity of the vortical structures are determined by the the size of the grid and the implicit artificial viscosity of the algorithm. The convective Mach number for the shear layer lies between 0.5 and 0.7, so the layer can be considered moderately compressible by the usual criteria.

The flow between the incident shock and the wedge is steady. Furthermore, the region between the shear layer and the Mach stem is subsonic in the vicinity of the triple point. A sonic line emanates from the triple point and moves along the shear layer. After some distance, the sonic line turns upward and ends up in the Mach stem. Beyond this pocket, the flow becomes supersonic and should have all the typical characteristics of planar detonations, such as formation of colliding triple points and transverse waves, and vorticity generation at the main front. Qualitatively, the results on the three different meshes are the same. Interestingly, the location of the explosion at the front is the same regardless of resolution. The results on the coarse meshes, however, are more diffuse than than the ones on the fine mesh, as expected. The shock profiles are more smeared, and the shear-layer structures, as well as the reaction zone, are not sufficiently resolved.

Since the equilibrium shock-polar admits a solution for the shock angle, β, it is expected that far downstream the Mach stem reduces to an oblique ZND wave, at an angle $\beta = 56.8°$. The instability mechanisms that were encountered in detonations in channel flows (Papalexandris 1997) and lead to the formation of triple points should also appear on the flow-field of oblique detonations. As demonstrated in the previous section, two-dimensional detonations are intrinsically unstable. This region, however, is too far downstream to be included in the computational domain.

For higher wedge angles, the equilibrium shock polar cannot give a solution for β. In such situations, a strong explosion of the main front is also expected to occur. Since there is no solution to the equilibrium shock-polar, the Mach stem cannot reduce to an oblique ZND wave downstream, and is everywhere curved. For even higher wedge angles, the shock-polars do not admit a solution, and the main front detaches from the wedge. Such high wedge angles have not been considered in the present work.

Case C

The activation energy is the same as in Case B, but the stiffness coefficient has now been increased:

$$E_a = 50 , \qquad K = 230.75 .$$

The wedge angle is $\theta = 20°$. The upstream velocity is $u_1 = 18.051$. The theoretical prediction is that, far downstream, the detonation will be a ZND wave with an overdrive factor of $f = 1.60$ and at an angle $\beta = 28.5°$. The equivalent channel-flow problem was examined in Case C in Papalexandris (1997). The computational domain consists of 1200×200 cells, corresponding to a nominal resolution of 8 points per half-reaction length of the one-dimensional, steady-state solution. As in case B, the shock turns smoothly until it reaches a steady state. Contour plots of the flow variables are given in Fig. 27a. These results are taken at time $t = 18.0$. No change in the flow variables could be observed after that time. The shock angle at the right boundary is very close to the asymptotic limit of $\beta = 28.5°$.

The case of a higher wedge angle, namely $\theta = 30°$, has also been considered. The computational domain consists of 1440×240 cells, corresponding to a nominal resolution of 8 points per half-reaction length. The upstream velocity is now set at $u_1 = 12.035$. Under this initial condition, the theoretical prediction is a detonation of overdrive factor $f = 1.6$, at a shock angle $\beta = 45.7°$. Results for this simulation, taken at time $t = 36.0$, are given in Fig. 27b. These results are similar to the ones obtained in the high-angle simulation of Case B. The basic features discussed above, *i.e.*, the explosion on the front, the development of an unsteady shear layer, and the formation of a subsonic pocket behind the Mach stem in the vicinity of the triple point, can also be observed in this simulation.

Li *et al.* (1994) also presented simulations for wedge-induced detonations using the flux-corrected-transport (FCT) algorithm, on a domain of 400×150 cells. Their numerical results seem to agree qualitatively with the results obtained with the proposed unsplit algorithm. In particular, they also observed that, for small wedge angles, the main front turns smoothly, while an explosion occurs at the front, if large wedge angles are considered. More detailed comparisons between the two studies cannot be made because Li *et al.* considered a different combustion model and did not use dimensionless quantities for their simulations.

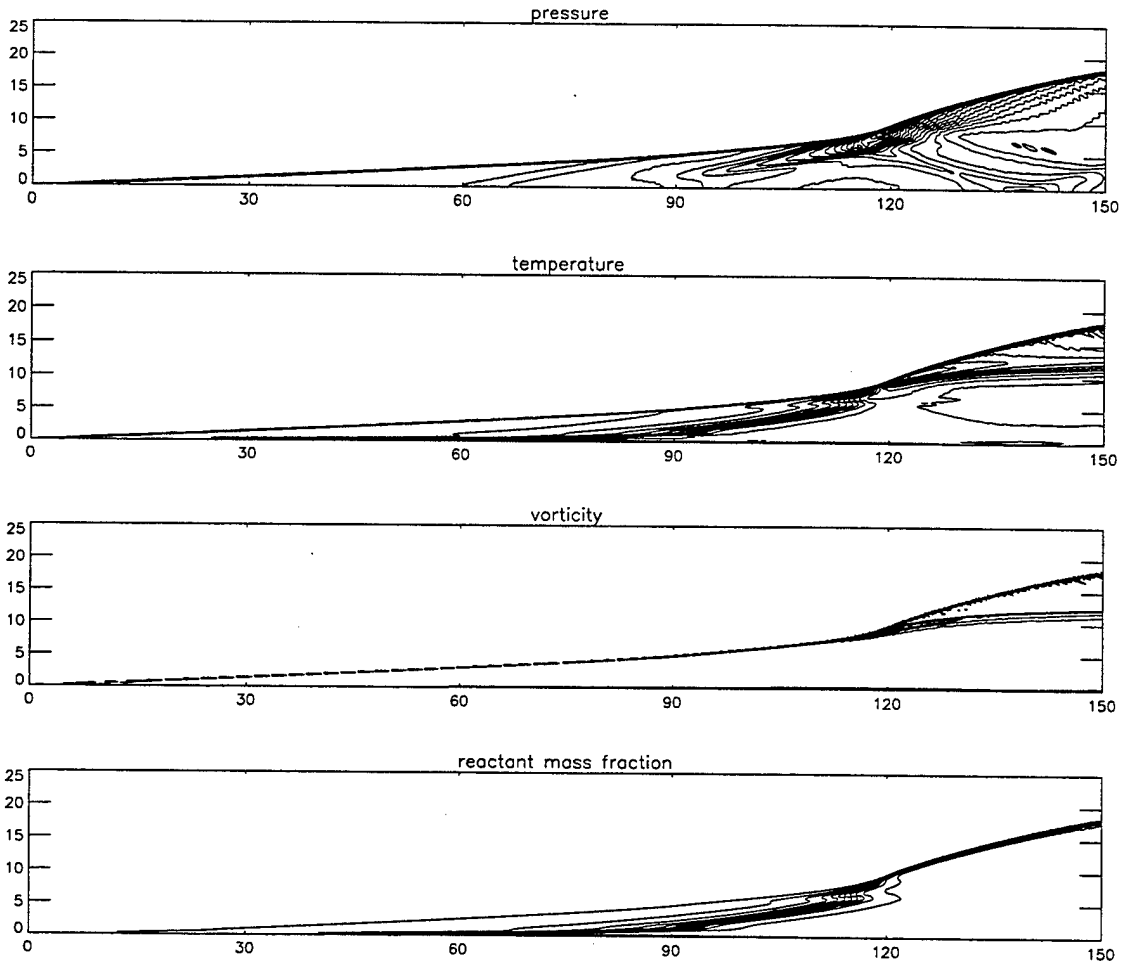

FIG. 27a Case C, $\theta = 20°$: contour plots of the flow variables at $t = 18.0$.

7.3 Detonations induced by short wedges

In the cases examined and discussed above, it was assumed that the wedge is long enough for the explosion to take place upstream of the corner of the wedge. In such cases, the location of the explosion and the flow-field in that neighborhood are determined completely by the kinetics of the reaction. If, however, the wedge is not long enough, then the explosion will take place near the corner. The effect of the corner in such situations has also been studied numerically, and the results are described below.

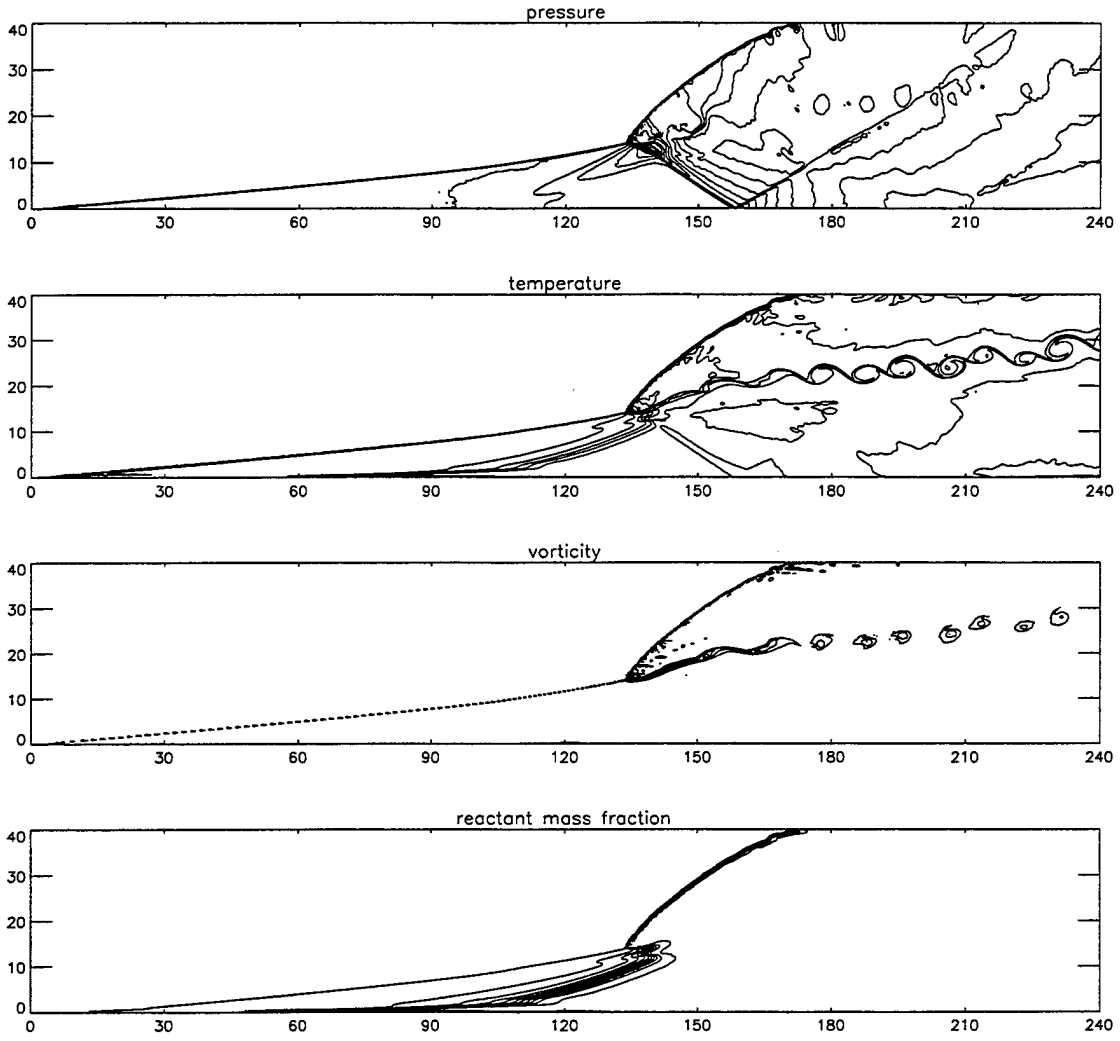

FIG. 27b Case C, $\theta = 35°$: contour plots of the flow variables at $t = 36.0$.

The heat release from the chemical reaction raises the temperature of the fluid, while the expansion at the corner decreases it. These two mechanisms "compete" against each other. Furthermore, including the downstream corner in the computational domain introduces a second characteristic length, the height of the wedge, h_w, into the dynamics, in addition to the half-reaction length. The combination of these two length-scales, with the wedge angle, θ, determines which of the two mechanisms will dominate.

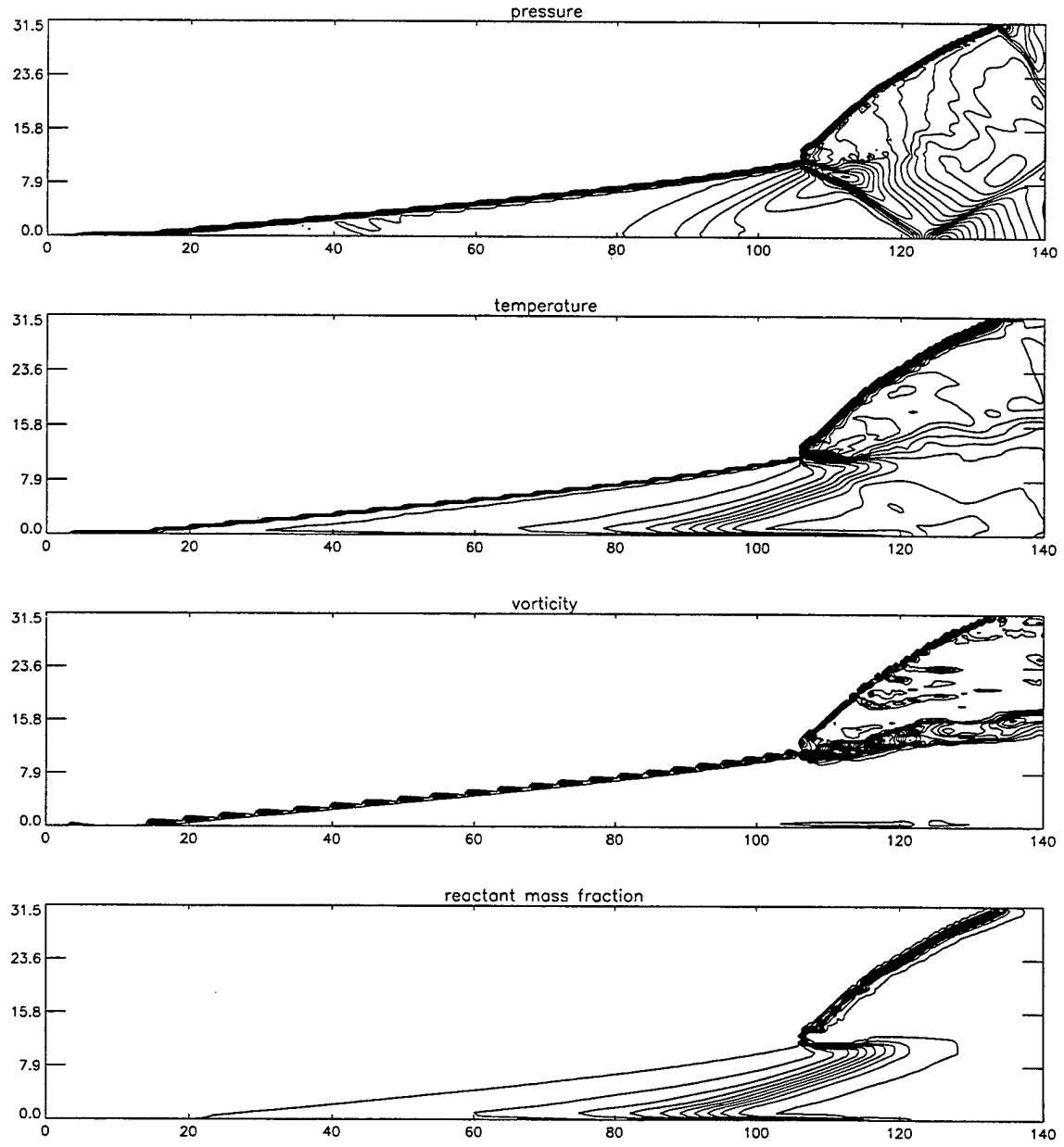

FIG. 26d Case B, $\theta = 35°$: contour plots of the flow variables at $t = 50.0$. Resolution, 280×64 cells.

In the numerical simulations, the activation energy and the stiffness coefficient are set at $E_a = 50$ and $K = 99.762$, respectively. The wedge angle is $\theta = 35°$. The upstream state of the fluid is

$$p_1 = 1.0 , \qquad \rho_1 = 1.0 , \qquad u_1 = 11.509 .$$

The flow produced by these parameters and upstream conditions in the case of a long wedge was examined above (*cf.* Fig. 26d).

Three wedge heights are considered. First, the wedge height is set at $h_w = 70.0$. The computational domain consists of 930×330 cells. The length of the domain is 155.0, and its width from the upper wall of the wedge is 55.0. Results for this simulation, at $t = 46.0$, are shown in Fig. 28a. In this case the explosion occurs upstream with respect to the corner. The expansion at the corner does not affect the explosion because the flow in the corner is supersonic. The leading shock is expected to be reduced far downstream to a C-J wave, as in one-dimensional detonations initiated by a moving piston that comes suddenly to rest.

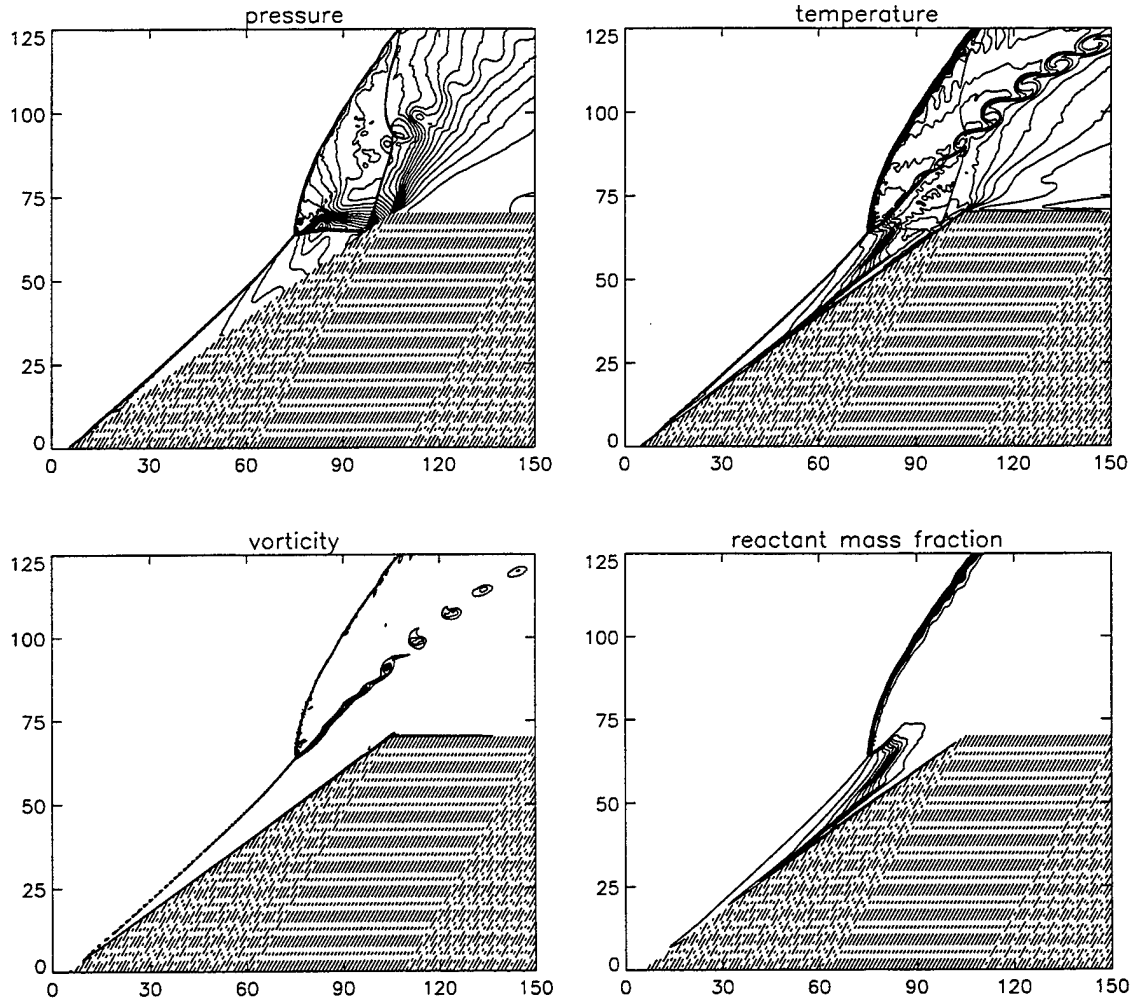

FIG. 28a Flow past a wedge of height $h_w = 70.0$ and angle $\theta = 35°$. Contour plots of the flow variables at $t = 46.0$.

The flow-field in the neighborhood of the inert shock and the explosion is the

same as in the corresponding case with a long wedge; see Fig. 26b. The interaction of the reflected shock with the shear layer causes the fluid to decelerate, thus forming another subsonic region in the flow-field, besides the one in the vicinity of the triple point. The expansion that takes place at the corner affects the evolution of the shear layer. As the fluid below the shear layer expands, the pressure and density drop, generating even higher entropy gradients across the layer. The expansion at the corner then leads to an increased amount of vorticity generation across the shear layer.

The wedge height was then reduced to $h_w = 50.0$. For this case, the computational domain consists of 810×420 cells. The length of the domain is 135.0 and its width, as measured from the upper wall of the wedge, is 70.0. Results from this simulation are shown in Fig. 28b, at time $t = 46.0$. In this case, the explosion takes place downstream of the corner. The flow in the subsonic area in the vicinity of the triple point (between the Mach stem and the shear layer) is influenced by the expansion at the corner. Additionally, the expansion at the corner affects the curvature of the leading front and the reflected shock.

A fluid element moving parallel to the wedge does not have time to increase its temperature substantially, via the thermal-runaway mechanism, because of the small length of the wedge. Consequently, it remains almost unreacted when it reaches the head of the expansion. The expansion produces a further decrease of the temperature, which delays the initiation of the reaction even more. Material on the upper wall of the wedge has remained only partially reacted (about 20%), as a result of the temperature decrease caused by the expansion at the corner.

As a final test, the wedge height is decreased further to $h_w = 25.0$. The simulation is performed on a domain of 1266×270 cells. The length of the domain is 210.0 and its width is 45.0. Results from this simulation, taken at $t = 10.0$, are presented in Fig. 28c. The expansion at the corner reduces the temperature so much that the gas near the wedge remains almost unreacted because the time needed for rapid reaction via thermal runaway becomes very large. As a result, a detonation cannot be established and the shock wave is expected to be reduced to a Mach wave, downstream. There is also a small pocket of slightly-reacted material near the wedge. Results from early times indicate that the formation of this pocket is a transient phenomenon caused by the interaction of the shock wave and the expansion at the corner, in the beginning of the simulation. The pocket is convected downstream with the fluid velocity. The minimum value of the reactant mass fraction inside the pocket is $z \simeq 0.9$. If the material reacted

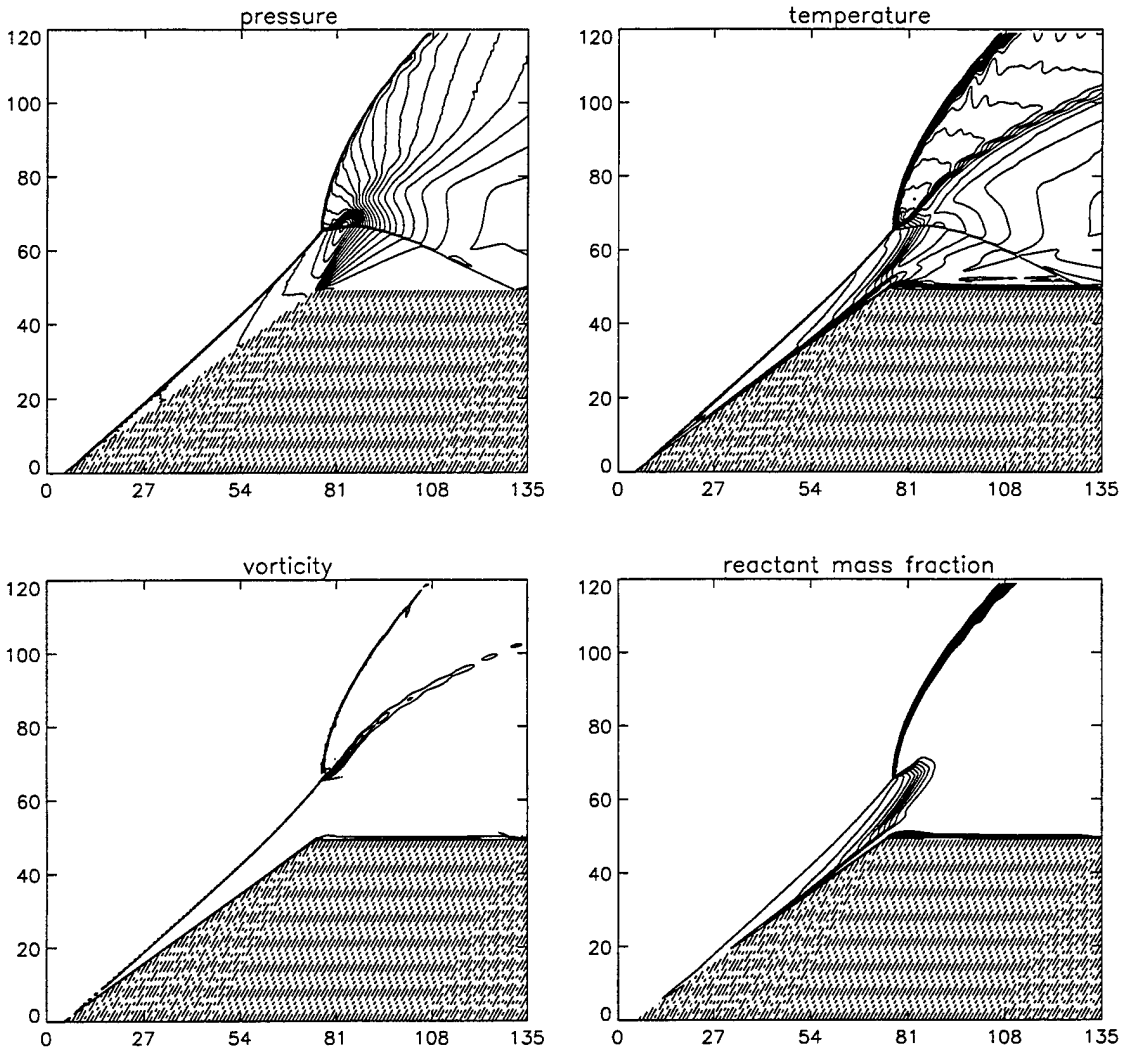

FIG. 28b Flow past a wedge of height $h_w = 50.0$ and angle $\theta = 35°$. Contour plots of the flow variables at $t = 46.0$.

completely, pressure waves would be transmitted to the shock wave, and a C-J detonation could be established. The reaction rate, $\dot{z} = -Kz\exp(-E_a/T)$, inside the pocket decays with time, however, indicating that the reaction process will not be completed there. After some time, the pocket exits the computational domain and the shock front assumes a fixed position. No change in the flow variables are subsequently observed. The material all along the wedge will remain only partially reacted and a detonation will not be established.

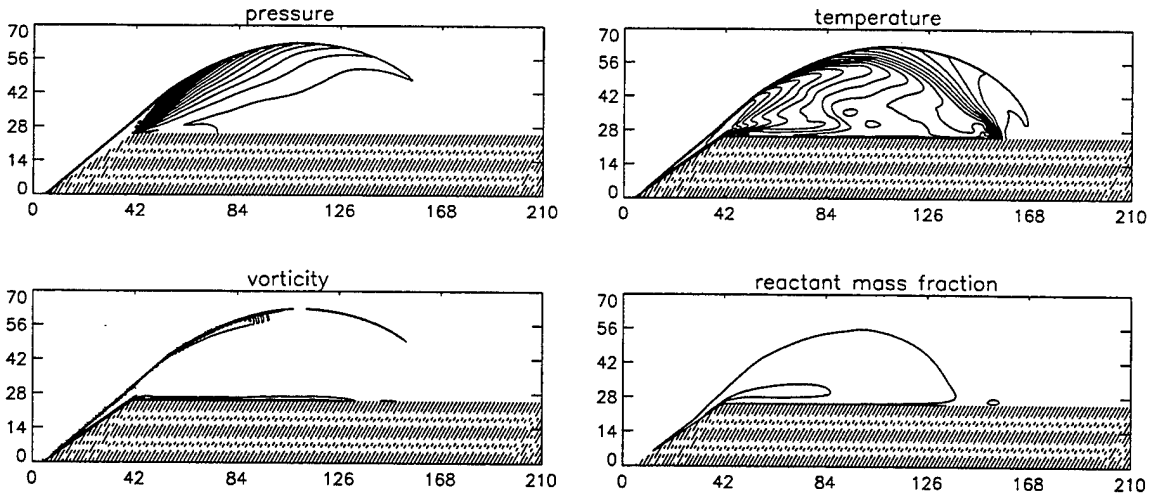

FIG. 28c Flow past a wedge of height $h_w = 25.0$ and angle $\theta = 35°$. Contour plots of the flow variables at $t = 10.0$.

7.4 Concluding remarks

The proposed unsplit numerical scheme has been used for the numerical study of two-dimensional detonating flows. The scheme is based on a decomposition of the governing equations that is mathematically consistent and appears capable of capturing important details of the structure of the resulting flow-fields, some of which have not been easy to simulate in the past. No explicit artificial viscosity mechanisms, or any other of the usual "fixes" (such as entropy-fixes or flux-splitting), have been employed.

With this scheme, it was verified that two-dimensional detonations propagating in narrow channels are intrinsically unstable and exhibit chaotic behavior (Papalexandris 1997). They are characterized by the presence of cellular patterns. These patterns are formed by the transverse waves of the triple points of the main front. The slip lines emanating from the triple points are rolled-up vortex sheets. They detach from the leading shock when triple-point collisions occur. Vortical structures are also generated by shock curvature, but their strength decreases substantially within the chemical reaction zone.

In addition to a host of detonation phenomena (Papalexandris 1997; Papalexandris, Dimotakis, and Leonard 1997a,b) a numerical study of shock-wedge induced detonations was also performed, as described above. These simulations demonstrated that, for small wedge angles, the shock attached to the wedge turns smoothly

to an oblique ZND wave. For high wedge angles, however, such a smooth turn is not possible and an explosion takes place at the front. The center of the explosion is a stationary triple point. A shear layer emanates from the triple point, that is hydrodynamically unstable.

The effect of the downstream corner of the wedge was also studied numerically. It was shown that when the explosion of the leading front takes place upstream of the corner, the expansion at the corner does not affect the evolution of the front, which reduces to a C-J wave. When the explosion occurs downstream of the corner, the curvature of the front and the reaction process depend on the expansion at the corner. It appears that for wedge heights small enough, a detonation cannot be established downstream, and the front decays downstream to a Mach wave.

8. References

ADRIAN, R. J. 1991 "Particle-Imaging Techniques for Experimental Fluid Mechanics," *Ann. Rev. Fluid Mech.* **23**, 261–304.

BARRON, J. L., FLEET, D. J. & BEAUCHEMIN, S. S. 1994 "Performance of Optical Flow Techniques," *Int. J. Comp. Vision* **12**, 43–77.

BOND, C. L. & DIMOTAKIS, P. E. 1993 "Molecular mixing in supersonic shear layers," *Bull. Am. Phys. Soc.* **38**(12), 2201.

BRADSHAW, P. 1966 "The effect of initial conditions on the development of a free shear layer," *J. Fluid Mech.* **26**(2), 225–236.

BROADWELL, J. E. & MUNGAL, M. G. 1991 "Large-scale structures and molecular mixing," *Phys. Fluids* A **3**(5), Pt. 2, 1193–1206.

BROWN, G. L. & ROSHKO, A. 1974 "On Density Effects and Large Structure in Turbulent Mixing Layers," *J. Fluid Mech.* **64**, 775–816.

BURKE, S. P. & SCHUMANN, T. E. W. 1928 "Diffusion Flames," *Ind. Eng. Chem.* **20**, 998.

CATRAKIS, H. J. & DIMOTAKIS, P. E. 1996a "Mixing in turbulent jets: scalar measures and isosurface geometry," *J. Fluid Mech.* **317**, 369–406.

CATRAKIS, H. J. & DIMOTAKIS, P. E. 1996b "Scale Distributions and Fractal Dimensions in Turbulence," *Phys. Rev. Lett.* **77**, 3795–3798.

CATRAKIS, H. J. & DIMOTAKIS, P. E. 1996c "Scale-dependent-fractal geometry," NATO Advanced Studies Institute series, *Mixing: Chaos and Turbulence*, GALCIT Report FM97–2.

CATRAKIS, H. J. & DIMOTAKIS, P. E. 1998 "Shape Complexity in Turbulence," *Phys. Rev. Lett.* **80**, 968–971.

CLEMENS, N.T. & MUNGAL, M.G. 1995 "Large-scale structure and entrainment in the supersonic mixing layer," *J. Fluid Mech.* **284**, 171–216.

COOK, A. W. 1998 "Large-eddy simulation of variable-density flows," submitted to the *J. Fluid Mech.* .

DAHM, W. J. A., SOUTHERLAND, K. B. & BUCH, K. A. 1991 "Direct, high resolution, four-dimensional measurements of the fine scale structure of $Sc \gg 1$ molecular mixing in turbulent flows," *Phys. Fluids A* **3**(5, Pt. 2), 1115–1127.

DAHM, W. J. A., SU, L. K. & SOUTHERLAND, K. B. 1992 "A scalar imaging velocimetry technique for fully resolved four-dimensinoal vector velocity measurements in turbulent flows," *Phys. Fluids A* **4**(10), 2191–2206.

DAHM, J. A., SU, L. K. & TACINA K. M. 1996 "Four-Dimensional Measurements of Vector Fields in Turbulent Flows," (invited paper) *AIAA* 27th *Fluid Dynamics Conference*, Paper 96–1987.

DIMOTAKIS, P. E. 1986 "Two-Dimensional Shear-Layer Entrainment," *AIAA J.* **24**, 1791–1796.

DIMOTAKIS, P. E. 1987 "Turbulent shear layer mixing with fast chemical reactions," *Turbulent Reactive Flows*. In, *Lecture Notes in Engineering* **40** (Ed. R. Borghi and S. N. B. Murthy, Springer-Verlag, New York, 1989), 417–485.

DIMOTAKIS, P. E. 1991a "Turbulent Free Shear Layer Mixing and Combustion," *High Speed Flight Propulsion Systems*, in *Progress in Astronautics and Aeronautics* **137**, Ch. 5, 265–340.

DIMOTAKIS, P. E. 1991b "On the convection velocity of turbulent structures in supersonic shear layers," *AIAA* 22nd *Fluid Dynamics, Plasma Dynamics and Lasers Conference*, Paper 91–1724.

DIMOTAKIS, P. E. 1993 "Some issues on turbulent mixing and turbulence," GALCIT Report FM93–1a.

DIMOTAKIS, P. E. & CATRAKIS, H. J. 1996 "Turbulence, fractals, and mixing," NATO Advanced Studies Institute series, *Mixing: Chaos and Turbulence*, GALCIT Report FM97–1.

DIMOTAKIS, P. E., CATRAKIS, H. J., COOK, A. W. & PATTON, J. M. 1998 "On the geometry of two-dimensional slices of irregular level sets in turbulent flows," 2nd *Monte-Verita Colloquium on Fundamental Problematic Issues in Turbulence*, 22–28 March 1998 (Ascona, Switzerland), GALCIT Report FM98–2.

DIMOTAKIS, P. E., CATRAKIS, H. J. & FOURGUETTE, D. C. 1998 "Beam Propagation and Phase-Front Integrals in High Reynolds Number Shear Layers and Jets," *AIAA* 29th *Plasmadynamics and Lasers Conference*, Paper 98–2833.

DIMOTAKIS, P. E. & HALL, J. L. 1987 "A simple model for finite chemical kinetics analysis of supersonic turbulent shear layer combustion," *AIAA/SAE/ASME/-ASEE* 23rd *Joint Propulsion Meeting*, Paper 87–1879.

EGOLFOPOULOS, F. N., DIMOTAKIS, P. E. & BOND, C. L. 1996 "On Strained Flames with Hypergolic Reactants: The $H_2/NO/F_2$ System in High-Speed, Supersonic and Subsonic Mixing-Layer Combustion," *Twenty-Sixth Symposium (International) on Combustion.* The Combustion Institute, Pittsburgh, 2885–2893.

GORNOWICZ, G. G. 1997 *Continuous-field Image-Correlation Velocimetry and its Application to Unsteady Flow Over an Airfoil*, California Institute of Technology, Aeronautical Engineer's thesis.

HALL, J. L., DIMOTAKIS, P. E. & ROSEMANN, H. 1991 "Some measurements of molecular mixing in compressible turbulent mixing layers," *AIAA* 22nd *Fluid Dynamics, Plasma Dynamics and Lasers Conference*, Paper 91–1719.

HALL, J. L., DIMOTAKIS, P. E. & ROSEMANN, H. 1993 "Experiments in non-reacting compressible shear layers," *AIAA J.* **31**, 2247–2254.

HO, C.-M. & HUANG, L.-S. 1982 "Subharmonics and vortex merging in mixing layers," *J. Fluid Mech.* **119**, 443–73.

HORN, B.K.P. & SCHUNCK, B.G. 1981 "Determining Optical Flow," *Artificial Intelligence* **17**, 185–203.

HUANG, M.-J. 1994 "Theoretical and Computational Studies of Isotropic Homogeneous Turbulence," California Institute of Technology, Ph.D. thesis.

ISLAND, T. C. 1997 "Quantitative Scalar Measurements and Mixing Enhancement in Compressible Shear Layers," Stanford HTGL Report No. TSD–104.

KARASSO, P. S. & MUNGAL, M. G. 1996 "Scalar mixing and reaction in plane liquid shear layers," *J. Fluid Mech.* **323**, 23–63.

KEE, R. J. 1991 pvte. communications.

KEE, R.J., MILLER, J.A., EVANS, G.H. & DIXON-LEWIS, G. 1988 *Twenty-Second Symposium (International) on Combustion.* The Combustion Institute, Pittsburgh, 1479–1494.

KEE, R. J., RUPLEY, F. M. & MILLER J.A. 1985 "Chemkin-II: A Fortran Chemical Kinetics Package for the Analysis of Gas-Phase Chemical Kinetics," Sandia Report SAND89–8009.

KEE, R. J., WARNATZ, J. & MILLER, J. A. 1983 "A FORTRAN Computer Code Package for the Evaluation of Gas-Phase Viscosities, Conductivities and Diffusion Coefficients," Sandia Report SAND83–8209.

KOOCHESFAHANI, M. M. & DIMOTAKIS, P. E. 1986 "Mixing and chemical reactions in a turbulent liquid mixing layer," *J. Fluid Mech.* **170**, 83–112.

LAPPAS, T. 1993 *An Adaptive Lagrangian Method for Computing 1-D Reacting Flows and the Theory of Riemann Invariant manifolds for the Compressible Euler Equations*, Ph.D. thesis, California Institute of Technology.

LAPPAS, T., LEONARD, A. & DIMOTAKIS, P. E. 1993 "An Adaptive Lagrangian Method for Computing 1-D Reacting and Non-Reacting Flows," *J. Comp. Phys.* **104**, 361–376.

LAPPAS, T., LEONARD, A. & DIMOTAKIS, P.E. 1998 "Riemann invariant manifolds for the multidimensional Euler equations," *SIAM J. Sci. Comp.* (accepted).

LI, C., KAILASANATH, K. & ORAN, E. S. 1994 "Detonation structures behind oblique shocks," *Phys. Fluids* **6**, 1600–1611.

LU, G. & LELE, S. K. 1994 "On the density ratio effect on the growth rate of a compressible mixing layer," *Phys. Fluids* **6**, 1073–1075.

PAPALEXANDRIS, M. V. 1997 *Unsplit Numerical Schemes for Hyperbolic Systems of Conservation Laws with Source Terms*, California Institute of Technology, Ph.D. thesis.

PAPALEXANDRIS, M. V., LEONARD, A., & DIMOTAKIS, P. E. 1997a "Unsplit Schemes for Hyperbolic Conservation Laws with Source Terms in One Space Dimension," *J. Comp. Phys.* **134**, 31–61.

PAPALEXANDRIS, M. V., LEONARD, A. & DIMOTAKIS, P. E. 1997b "Unsplit schemes for multi-dimensional systems of hyperbolic conservation laws with source terms," *J. Comp. Phys.* (submitted).

PAPAMOSCHOU, D. 1989 "Structure of the compressible turbulent shear layer," *AIAA* 27$^{\text{th}}$ *Aerospace Sciences Meeting*, Paper 89–0126.

PEARLSTEIN, A. J. & CARPENTER, B. N. 1995 "On the determination of solenoidal or compressible velocity fields from measurements of passive or reactive scalars," *Phys. Fluids A* **7**(4), 754–763.

REYNOLDS, W. C. 1986 "The Element Potential Method for Chemical Equilibrium Analysis: Implementation in the Interactive Program STANJAN, Version 3," Mechanical Engineering, Stanford (January 1986).

SHOLL, M. & SAVAS, Ö. 1997 "A Fast Lagrangian PIV Method for Study of General High-Gradient Flows," *AIAA* 35$^{\text{th}}$ *Aerospace Sciences Meeting*, Paper 97–0493.

SLESSOR, M. D. 1998 *Aspects of turbulent-shear-layer dynamics and mixing*, Ph.D. thesis, California Institute of Technology.

SLESSOR, M. D., BOND, C. L. & DIMOTAKIS, P. E. 1998 "Turbulent shear-layer mixing at high Reynolds numbers: effects of inflow conditions," *J. Fluid Mech.* (accepted). GALCIT Report FM98–1.

SLESSOR, M. D., ZHUANG, M. & DIMOTAKIS, P. E. 1998 "Turbulent shear-layer mixing: growth-rate compressibility scaling," GALCIT Report FM98–9.

SU, L. K. & DAHM, W. J. A. 1995 *Scalar Imaging Velocimetry and Its Application in Measurements of the Structure and Dynamics of the Complete Velocity Gradient Tensor in Turbulent Flows*, Ph.D. thesis, University of Michigan.

SZELISKI, R. & SHUM, H. 1996 "Motion Estimation with Quadtree Splines," *IEEE Trans. Pattern Matching and Machine Intelligence* **18**(12), 1199–1210.

TOKUMARU, P. T. & DIMOTAKIS, P. E. 1995 "Image Correlation Velocimetry," *Exps. in Fluids* **19**(1), 1–15.

WILLERT, C.E. & GHARIB, M. 1991 "Digital partical image velocimetry," *Exps. in Fluids* **10**, 181–193.

WILLICK, D. & YANG, Y.-H. 1991 "Experimental Evaluation of Motion Constraint Equations," *CVGIP: Image Understanding* **54**(2), 206–214.

ZHOU, Z., SYNOLAKIS, C. E., LEAHY, R. M. & SONG, S. M. 1995 "Calculation of 3D internal displacement fields from 3D X-ray computer tomographic images," *Proc. Roy. Soc. London* A **449**, 537–554.

9. Personnel

9.1 Personnel supported by this effort

- Bond, C. L., Graduate Research Assistant, Aeronautics.
- Catrakis, H. J., Research Fellow, Aeronautics.
- Chase, Stephen, Undergraduate Research Assistant.
- Dahl, E. E., Member of the Technical Staff, Aeronautics.
- Dimotakis, P.E., John K. Northrop Professor of Aeronautics & Professor of Applied Physics (PI).
- Fourguette, D. C., Senior Research Fellow, Aeronautics.‡
- Gornowicz, G. G., Graduate Research Assistant, Aeronautics.♯
- Lang, D. B., Research Engineer, Aeronautics.
- Leonard, A., Professor, Aeronautics (Co-PI).
- Papalexandris, M. V., Graduate Research Assistant, Aeronautics.*
- Shan, J. W., Graduate Research Assistant, Aeronautics.
- Shekar, Kiran, Undergraduate Research Assistant.
- Slessor, M. D., Graduate Research Assistant, Aeronautics.
- Svitek, P., Staff Engineer.

---

‡ Through Nov 1996. Presently with Rice Systems, Inc.

♯ Through June 1997. Presently with DreamWorks SKG (Glendale, CA).

* Presently with the Jet Propulsion Laboratory.

9.2 Other collaborators

- Cook, A. W., Lawrence Livermore National Laboratory.
- Cook, Grant, Lawrence Livermore National Laboratory.
- Collins, S. A., JPL (digital imaging).
- Egolfopoulos, F. N., Associate Professor, Mech. Eng., USC.
- Henderson, R., Sr. Research Fellow, Aeronautics and Applied Mathematics, Caltech.
- Elliot, T., JPL (digital imaging).
- Martin, C., Prof. Physics, Caltech.
- Meiron, D. I., Applied Mathematics, Caltech.
- Miller, P. L., Lawrence Livermore National Laboratory.
- Wadsworth, M., JPL (digital imaging).

10. Publications of work supported by this Grant

Publications and reports submitted, accepted, or published of work performed under sponsorship of this grant:

BOND, C. L. & DIMOTAKIS, P. E. 1996 "Molecular mixing in high Reynolds number, subsonic, free shear layers," Fall Technical Meeting, Western States Section (Combustion Institute), 28–29 October 1996 (U. So. California), Paper 96F–099.

BOND, C. L., SLESSOR, M. D. & DIMOTAKIS, P. E. 1997 "Measurements of molecular mixing in subsonic high-Reynolds-number shear layers," *Am. Phys. Soc.* 50^{th} *Annual Meeting, Division of Fluid Dynamics* (San Francisco, CA, 23–25 November 1997).

CATRAKIS, H. J. 1996 *Mixing and the Geometry of Isosurfaces in Turbulent Jets*, Ph.D. thesis, California Institute of Technology.

CATRAKIS, H. J. & DIMOTAKIS, P. E. 1996a "Mixing in turbulent jets: scalar measures and isosurface geometry," *J. Fluid Mech.* **317**, 369–406.

CATRAKIS, H. J. & DIMOTAKIS, P. E. 1996b "Scale Distributions and Fractal Dimensions in Turbulence," *Phys. Rev. Lett.* **77**, 3795–3798.

CATRAKIS, H. J. & DIMOTAKIS, P. E. 1996c "Scale-dependent-fractal geometry," NATO Advanced Studies Institute series, *Mixing: Chaos and Turbulence*, GALCIT Report FM97–2.

CATRAKIS, H. J. & DIMOTAKIS, P. E. 1998 "Shape Complexity in Turbulence," *Phys. Rev. Lett.* **80**, 968–971.

DIMOTAKIS, P. E. 1997 "Non-premixed hydrocarbon flame," *Nonlinearity* **7**, 1–2.

DIMOTAKIS, P. E. & CATRAKIS, H. J. 1996 "Turbulence, fractals, and mixing," NATO Advanced Studies Institute series, *Mixing: Chaos and Turbulence*, GALCIT Report FM97–1.

DIMOTAKIS, P. E., CATRAKIS, H. J., COOK, A. W. & PATTON, J. M. 1998a "On the geometry of two-dimensional slices of irregular level sets in turbulent flows," 2nd *Monte-Verita Colloquium on Fundamental Problematic Issues in Turbulence*, 22–28 March 1998 (Ascona, Switzerland), GALCIT Report FM98–2.

DIMOTAKIS, P. E., CATRAKIS, H. J. & FOURGUETTE, D. C. 1998b "Beam Propagation and Phase-Front Integrals in High Reynolds Number Shear Layers and Jets," *AIAA* 29th *Plasmadynamics and Lasers Conference*, Paper 98–2833.

EGOLFOPOULOS, F. N., DIMOTAKIS, P. E. & BOND, C. L. 1996 "On Strained Flames with Hypergolic Reactants: The $H_2/NO/F_2$ System in High-Speed, Supersonic and Subsonic Mixing-Layer Combustion," *Twenty-Sixth Symposium (International) on Combustion*. The Combustion Institute, Pittsburgh, 2885–2893.

EGOLFOPOULOS, F. N. & DIMOTAKIS, P. E. 1998 "Non-premixed hydrocarbon ignition at high strain rates," *Twenty-Seventh Symposium (International) on Combustion*, Paper 5C11. GALCIT Report FM98–7.

GORNOWICZ, G. G. 1997 *Continuous-field Image-Correlation Velocimetry and its Application to Unsteady Flow Over an Airfoil*, California Institute of Technology, Aeronautical Engineer's thesis.

GORNOWICZ, G. G. & DIMOTAKIS, P. E. 1995 "Continuous-field image correlation velocimetry," *Bull. Am. Phys. Soc.* **40**(12), 2000.

LAPPAS, T., LEONARD, A. & DIMOTAKIS, P.E. 1998 "Riemann invariant manifolds for the multidimensional Euler equations," *SIAM J. Sci. Comp.* (accepted).

PAPALEXANDRIS, M. V. 1997 *Unsplit Numerical Schemes for Hyperbolic Systems of Conservation Laws with Source Terms*, California Institute of Technology, Ph.D. thesis.

PAPALEXANDRIS, M. V., LEONARD, A. & DIMOTAKIS, P. E. 1995 "An unsplit scheme for 1-D unsteady chemically-reacting flows," *SIAM Annual Meeting* (23–26 October 1995, Charlotte, NC), to appear.

PAPALEXANDRIS, M. V., LEONARD, A., & DIMOTAKIS, P. E. 1996 "Unsplit Schemes for Hyperbolic Conservation Laws with Source Terms in One Space Dimension," California Institute of Technology, GALCIT Report FM96–1.

PAPALEXANDRIS, M. V., LEONARD, A., & DIMOTAKIS, P. E. 1997 "Unsplit Schemes for Hyperbolic Conservation Laws with Source Terms in One Space Dimension," *J. Comp. Phys.* **134**, 31–61.

PAPALEXANDRIS, M. V., LEONARD, A. & DIMOTAKIS, P. E. 1997 "Unsplit schemes for multi-dimensional systems of hyperbolic conservation laws with source terms," *Am. Phys. Soc.* 50^{th} *Annual Meeting, Division of Fluid Dynamics* (San Francisco, CA, 23–25 November 1997).

PAPALEXANDRIS, M. V., LEONARD, A. & DIMOTAKIS, P. E. 1997 "Unsplit schemes for multi-dimensional systems of hyperbolic conservation laws with source terms," *J. Comp. Phys.* (submitted).

SHAN, J. W., LAIDLAW, D. H., GORNOWICZ, G. G., LANG, D. B. & DIMOTAKIS, P. E. 1997 "Three-dimensional space-time structure of turbulent jets," *Am. Phys. Soc.* 50^{th} *Annual Meeting, Division of Fluid Dynamics* (San Francisco, CA, 23–25 November 1997).

SLESSOR, M. D. 1998 *Aspects of turbulent-shear-layer dynamics and mixing*, Ph.D. thesis, California Institute of Technology.

SLESSOR, M. D., BOND, C. L. & DIMOTAKIS, P. E. 1998 "Turbulent shear-layer mixing at high Reynolds numbers: effects of inflow conditions," *J. Fluid Mech.* (accepted). GALCIT Report FM98–1.

SLESSOR, M. D. & DIMOTAKIS, P. E. 1994 "Experiments on bi-supersonic turbulent shear layers," *Bull. Am. Phys. Soc.* **39**(9), 1880.

SLESSOR, M. D. & DIMOTAKIS, P. E. 1995 "Some new compressible mixing-layer experiments," *Bull. Am. Phys. Soc.* **40**(12), 1975.

SLESSOR, M. D., ZHUANG, M. & DIMOTAKIS, P. E. 1998 "Turbulent shear-layer mixing: growth-rate compressibility scaling," GALCIT Report FM98–9.

TOKUMARU, P. T. & DIMOTAKIS, P. E. 1995 "Image Correlation Velocimetry," *Exps. in Fluids* **19**(1), 1–15.

11. Interactions/transitions

Visits/interactions/participation/presentations at meetings, conferences, seminars:

- Fokion N. Egolfopoulos (USC): Discussions and collaborations on strained-flame numerical simulations and hydrocarbon ignition (continuous throughout the year).
- Stefan Deusch (ETH, Zurich): Discussions on Image Correlation Velocimetry methodology (November 1996 visit).
- H. C. Catrakis, P. E. Dimotakis, M. D. Slessor, A. Leonard: Attended 49th APS/DFD meeting (Syracuse, NY), 24-26 November 1996 (2 presentations of work sponsored under this Grant).
- P. Dimotakis: "Turbulent mixing in high-speed shear-layer flows," GALCIT Seminar (10 January 1997), Arizona S.U. (March 97), and U.C. San Diego (26 August 1997).
- A. Leonard: "LES model for scalar transport." Invited talk, AIAA (Reno, NV, January 97). Also, later, at U.C. Irvine, and U.C. Santa Barbara.
- M. V. Papalexandris: "Unsplit numerical scheme for hyperbolic systems of equations," GALCIT seminar (9 May 1997).
- A. Leonard: "Recent advances in high-resolution vortex methods for incompressible flows," invited talk, AIAA 13th CFD Conference (Snowmass, Colorado, 29 June - 2 July 1997).

- Prof. H. Lam (Princeton U.): Discussions on reduced-chemistry methods for numerical simulation of chemically-reacting flows (4–8 August 1997 visit to Caltech).
- Prof. Paul Clavin (U. Marseilles): Discussions on detonation (August 1997 visit by P. Dimotakis to UCSD).
- Prof. Amable Liñan (Spain): Discussions on turbulent mixing (August 1997 visit by P. Dimotakis to UCSD).
- Prof. Forman Williams (UCSD): Discussions on turbulent mixing, energy equation in chemically-reacting flows, detonations (August 1997 visit by P. Dimotakis to UCSD).

Consultative and advisory functions to other labs, agencies, especially AF and DoD (include institutions, locations, dates, names):

- P. E. Dimotakis: Lawrence Livermore National Laboratories. Consulting on compressible turbulence, inertial-confinement fusion, high-fluence laser-doubling crystal growth.
- P. E. Dimotakis: Member and participation throughout the last 12 months in NAS/NRC Committee that reviewed DOE's Inertial Confinement Fusion Program and the National Ignition Facility.
- P. E. Dimotakis: Membership to DOD/Mitre/JASON group (Meetings, July 1997).

Transitions (cases where knowledge resulting from this research is used or will be used in a technology application):

None

New Discoveries, inventions, patents:

None

12. Honors/awards

Honors, degrees, and awards received during period, as well as, 'lifetime achievement honors such as Nobel prize, honorary doctorates, and society fellowships prior to this effort':

- Catrakis, H. J.:
  - Ph.D., California Institute of Technology (June 1996).
  - Assistant Professor, U. C. Irvine (starting July 1998).
- Dimotakis, P. E.:
  - John K. Northrop Chair, Aeronautics, Caltech (February 1995).
  - Associate Fellow, AIAA (June 1989).
  - Fellow, Am. Phys. Society (November 1980).
- Gornowicz, G. G.:
  - A.E., California Institute of Technology (June 1997).
- Leonard, A.:
  - Fellow, Am. Phys. Society.
  - Vice-Chair, Am. Phys. Society, Division of Fluid Dynamics (1997).
  - Chair, Am. Phys. Society, Division of Fluid Dynamics (1998).
- Papalexandris, M. V.:
  - Ph.D., California Institute of Technology (June 1997).
- Slessor, M. D.:
  - Ph.D., California Institute of Technology (June 1998).